Hydrodynamics and Nucleosynthesis of Jet-Driven Supernovae II: Comparisons with Abundances of Extremely Metal-Poor Galaxies and Constraints on Supernova Progenitors

Shing-Chi Leung[1] and Ken'ichi Nomoto[2]

[1]*Department of Mathematics and Physics, SUNY Polytechnic Institute, 100 Seymour Road, Utica, NY 13502, USA*

[2]*Kavli Institute for the Physics and Mathematics of the Universe (WPI), The University of Tokyo Institutes for Advanced Study, The University of Tokyo, Kashiwa, Chiba 277-8583, Japan*

ABSTRACT

The spectra of several galaxies, including extremely metal-poor galaxies (EMPGs) from the EM-PRESS survey, have shown that the abundances of some Si-group elements differ from "spherical" explosion models of massive stars. This leads to the speculation that these galaxies have experienced supernova explosions with high asphericity, where mixing and fallback of the inner ejecta with the outer material leads to the distinctive chemical compositions. In this article, we consider the jet-driven supernova models by direct two-dimensional hydrodynamics simulations using progenitors about $20 - 25\ M_\odot$ at zero metallicity. We investigate how the abundance patterns depend on the progenitor mass, mass cut and the asphericity of the explosion. We compare the observable with available supernova and galaxy catalogs based on ^{56}Ni, ejecta mass, and individual element ratios. The proximity of our results with the observational data signifies the importance of aspherical supernova explosions in chemical evolution of these galaxies. Our models will provide the theoretical counterpart for understanding the chemical abundances of high-z galaxies measured by the James Webb Space Telescope.

1. INTRODUCTION

1.1. *Simulations of Jet-Driven Supernovae*

Aspherical explosion is more likely for low metallicity stars. Due to the lack of metals for line absorption, the mass loss rate of these stars is suppressed (e.g., Marigo et al. 2001). The star tends to preserve the envelope and the total angular momentum (e.g., Murphy et al. 2021). When the star collapses, the preserved angular momentum may leave behind a rapidly rotating neutron star or black hole. Such highly rotating compact objects, combined with magnetic field, can trigger the magneto-hydrodynamical instability of the accretion disk. The disk can lead to a jet outburst which supplies a tremendous amount of energy ($\sim 10^{51}$ erg) to the envelope. This process is particularly important because massive stars with a mass $\geqslant 18\ M_\odot$ might explode as a hypernova (Nomoto et al. 2013).

The cone-shaped energy deposition creates a very different thermodynamical history for the explosive nucleosynthesis. This creates enhanced production around $A = 45, 65$ (e.g., Nagataki et al. 1997). The high temperature creates the alpha-rich freezeout, which is essential for producing individual isotopes such as ^{44}Ca, $^{47-48}$Ti, ^{59}Co (e.g., Maeda et al. 2002). Similar results are observed for the zero-metallicity star explosion performed in Tominaga (2009). The jet energy deposition triggers aspherical mass ejection, which can explain the carbon-enriched metal-poor stars (CEMPs) (Tominaga et al. 2007a), and some Zn-rich stars such as HE 1327-2326 (Ezzeddine et al. 2019). The jet structure also favours the ejection of ^{56}Ni-rich matter with a high velocity (Nagataki et al. 1998; Mazzali et al. 2005; Maeda et al. 2006), which has been observed in some supernovae and hypernovae (e.g. SN 1987A, SN 1998bw). The en-

Corresponding author: Shing-Chi Leung

leungs@sunypoly.edu

ergy composition of the jet also leaves signature by the polarization of the ejecta (e.g., Couch et al. 2009).

1.2. *Spectroscopic Observations*

The search of high redshift galaxies has opened another dimension in understanding the nature of supernova explosions, especially low metallcity ones. Similar to extremely metal-poor stars, extremely metal-poor galaxies (EMPGs) are ideal candidates to capture the effects of early massive supernova explosion by their chemical composition, which reflects the explosive yield of one or a few supernova explosions (e.g., Hartwig et al. 2018). Such early galaxies also imply that the Type Ia supernovae are less important, which have a delay time from the formation of white dwarfs to their final explosions (e.g., Kobayashi et al. 2020). Thus the composition of these extreme metal-poor objects provides direct constraints on the massive star explosion yields. Recent surveys, and their follow-up observations, have discovered several galactic objects with unusual Si- and Fe-group elements, including Ne, Si, S, Ar, Fe, and Ni.

In Kojima et al. (2020) the Extremely Metal-Poor Representatives Explored by the Subaru Survey (EMPRESS) is designed to use the Subaru/Hyper Supreme-Cam (HSC) optical images to identify the faint EMPGs. Among the > 100 EMPGs identified, their follow-up project later selected 13 galaxies and studied them in details, where the galaxies have a metallicity $Z \sim 0.1 - 1\% Z_\odot$ (Isobe et al. 2022). They measured the α-chain elements O, Ne, Ar and Fe, which can be directly connected to the massive star progenitors and explosion mechanisms. Among all features, these galaxies have the [Ne/O], [Ar/O] and [Fe/O] values very close to solar values or mildly sub-solar, despite their high metal-poor nature.

In Watanabe et al. (2023), the 13$^{\text{th}}$ follow-up project on the analysis of the galaxy catalogue from EMPRESS project is reported for more EMPGs, including SBS-0335-052E (Izotov et al. 2018), J2314+0154 (Kojima et al. 2020), and J0125+0759 (Kojima et al. 2020). The spectra of these galaxies are measured by Keck/LRIS. Ratios of [Ne/O], [Ar/O], [S/O] and [Fe/O] are reported. In that work, the mixing-fallback model is extensively adopted to explain the unconventional abundance pattern. These galaxies are shown to fit with a small mixing ratio, about $0 - 0.2$, however, the [Fe/O] cannot be fully explained by the mixing and fallback mechanisms. [Ar/O] and [S/O] could be indicators of PISN explosions.

1.3. *Motivation*

The chemical abundances provide first hand constraints on how massive stars explode and eject mat-

ter to the surrounding. The discrepancies between the measured galaxies' chemical abundance and nucleosynthesis yields of ordinary stars have led to comparisons with less canonical supernova models, including hypernovae and pair-instability supernova models (Isobe et al. 2022). While the early galaxies favour the formation of very massive stars (e.g., Hirano et al. 2015), later radiation hydrodynamics simulations suggest ordinary massive stars (see e.g., Latif et al. 2022). This implies that both ordinary and very massive stars are possible candidates for the chemical origin of these galaxies. The mismatch of chemical abundances of these galaxies with nucleosynthetsis yields of spherical models leads to the question, if aspherical explosion models can improve the matching.

For one-dimensional modeling, the mixing-fallback model has been often invoked to mimic the multi-dimensional mixing process (Umeda & Nomoto 2002). The mixing-fallback approximation has successfully explained the peculiar abundance patterns of some metal-poor stars, such as the very high C/Fe abundance ratio (e.g., Umeda & Nomoto 2002; Ishigaki et al. 2018).

In Paper I (Leung et al. 2023), we presented a catalogue of the jet-driven supernova models using multi-dimensional simulations. The model uses the 40 $M_\odot$ zero metallicity star as the progenitor. We studied nucleosynthesis of the jet-triggered explosion and showed how the chemical composition depends on the jet energetics. The yields of the jet models exhibit significant differences from spherical explosion models. The jet explosion is essential in reproducing the trend of some element pair such as Ti and V. It is therefore interesting to extend our models, and check if the results derived from a more consistent modeling provide better fitting.

In this article, we first review the essential massive star models presented in this work in Section 2. We describe how the massive star explosion models are prepared in both one- and two-dimensions. Then in Section 3 we present how the hydrodynamics and nucleosynthesis depend on the dimensionality, progenitor mass and other input physics. In Section 4 we analyze the elemental trends of some key element pairs, and compare them with the observed metal-poor stars and supernovae. We also present the elemental yields of our models. We apply our results to compare with some well-observed metal-poor galaxies, and some metal-poor stars in Section 5. At last we give our conclusion.

This article uses the convention

$$[X/Fe] = \log_{10} \frac{(X/Fe)}{(X/Fe)_\odot}. \tag{1}$$

2. MASSIVE STAR MODELS

2.1. Two-dimensional Simulations

In Paper I (Leung et al. 2023), we studied the dependence of explosive nucleosynthesis on the jet explosion parameters for the 40 $M_\odot$ star progenitor using the special relativistic hydrodynamics solver extended from Leung et al. (2015). The jet energy deposition rate, its duration, and the open angles are treated as main parameters. We followed Tominaga (2009) and set the *standard* jet as $\dot{E}_{\mathrm{dep},0} = 1.2 \times 10^{53}$ ergs^{-1}, $E_{\mathrm{dep},0} = 1.5 \times 10^{52}$ erg and a jet open angle of $15°$. This implies a jet deposition time of $t_{\mathrm{jet},0} = 0.125$ s.

In each model, we first remove the core material interior to the *mass cut*, and then we deposit the energy at the inner boundary of the jet with the jet prescription above. We adopt the Helmholtz equation of state (Timmes & Arnett 1999; Timmes & Swesty 2000) and a simple 7-isotope network (Timmes et al. 2000) to describe nuclear reactions in the hydrodynamics simulations. We calculate the explosion until most exothermic nuclear reactions have terminated and the ejecta appears to be in homologous expansion to a good approximation.

In the simulations, we use the tracer particle scheme (Arnett et al. 1989; Hachisu et al. 1990; Travaglio et al. 2004; Seitenzahl et al. 2010) to record the thermodynamic history of the underlying fluid motion. After the hydrodynamics simulations, we use the thermodynamic histories of the tracer particles to reconstruct the detailed nucleosynthesis with the 495-isotope network containing isotopes from H to Tc (Timmes 1999).

We extend our calculation to include progenitors with the zero-age main-sequence (ZAMS) masses of $M_{\mathrm{ZAMS}} = 20$ and 25 $M_\odot$ presented in Tominaga et al. (2007b). Recent pre-supernova and core-collapse models (e.g., Sukhbold et al. 2016) have demonstrated the possibilities the formation of an accretion disk and a following outburst. This also agrees with the suggestions by Nomoto et al. (2013) that the final fate of stars with a mass $M_{\mathrm{ZAMS}} \geqslant 25$ $M_\odot$ can bifurcate into faint supernovae and hypernovae following fallback. In Tables 1, 2, 3, and 4 we list the new models computed in this work and some of their essential parameters. For convenience we name all the models in the following format: a S20-0500-2000-15 corresponds to the progenitor model with $M_{\mathrm{ZAMS}} = 20 M_\odot$, the jet with the energy deposition rate of 0.5 $\dot{E}_{\mathrm{jet},0}$, jet deposition time of 2.0 $t_{\mathrm{jet},0}$, an open angle of $15°$. All models assume the inner boundary at 900 km, except for the series S25b (S25c) corresponds to the model sequences where the innermost boundary is located at 1500 (2100) km.

In Figure 1 we plot the tracer distribution of the characteristic model using the 25 $M_\odot$ star progenitor. We use the final energy of the tracers to determine if they are ejected or bound. The Si layer within the cone shape is ejected. The inner C+O layer has an increasing spread in the ejecta angular range until ~ 20000 km. Beyond that, the outer shell is ejected.

We summarize the tracer thermodynamic history in Figure 2. It collects the statistics of the passive tracers in the characteristic model when the tracers reach their maximum temperature. We bin the tracers according to their corresponding density. In the figure, the data points corresponds to the average of the tracers within individual density bins and the error bars stand for the standard deviation of the data.

The thermodynamics provides a useful diagnosis to the nuclear reaction class where the tracers have experienced. In general, high density and temperature burning leads to nuclear statistical equilibrium (NSE), where the composition can be solely determined by ρ, T, and Y_e. In NSE, the final composition can be predicted by the density where the matter leaves NSE. On the other hand, for a low density and high temperature environment, α-burning becomes the bottleneck of the entire nuclear reaction network. Thus, not all isotopes are equally accessible as in NSE. This gives rise to a unique chemical abundance pattern featuring high entropy isotopes, e.g., ^{64}Zn.

In the characteristic model of the 25 $M_\odot$ star, we observe an almost monotonically increasing trend for the tracers. Tracers in the inner part of the star, having higher densities, experienced higher peak temperatures in their burning history. There are observable fluctuations for tracers from the inner ejecta. It is because the ejecta includes both the region directly excited by the jet, and the nearby region which follows the expansion. Matter in the outer region is mostly ejected without experiencing a significant shock heating. The spherical-like mass ejection agrees with the low fluctuations among tracers.

In Figure 3 we plot the characteristic model using the 25 $M_\odot$ progenitor. The two-dimensional model shows a flat distribution of chemical elements from C to Zn. Most elements along the α-chain have abundances compatible with the solar abundance. Odd number elements such as P, K, Sc, and the low-Ye isotopes (i.e., the isotopes with a higher neutron number) are mostly underproduced. The zero-metallicity environment does not contain any ^{22}Ne to directly produce the low-Ye isotopes, especially in the Si-group elements.

2.2. Mixing-Fallback Mechanisms

The Mixing-Fallback model (Umeda & Nomoto 2002) is an approximate modeling of the jet-like aspherical

Table 1. The jet-driven supernova models using the 20 $M_\odot$ ZAMS star as the progenitor. $M_{\rm ZAMS}$, $M_{\rm pro}$ and $M_{\rm ej}$ are the progenitor ZAMS, pre-collapse and ejecta masses in units of $M_\odot$. $\dot{E}_{\rm dep}$, $t_{\rm dep}$ and $E_{\rm dep}$ are the energy deposition rate, deposition time and total deposited energy in units of the characteristic model. [Ne/O], [Si/O], [S/O], [Ar/O] and [Fe/O] are the $\log_{10}$ values of the ejecta mass fraction ratios of the element pairs, defined in solar values.

Model	$M_{\rm ZAMS}$	$M_{\rm pro}$	$\dot{E}_{\rm dep}$	$t_{\rm dep}$	$E_{\rm dep}$	$\theta_{\rm jet}$	$M_{\rm ej}$	[Ne/O]	[Si/O]	[S/O]	[Ar/O]	[Fe/O]
S20-0500-0500-15	20	4.08	0.50	0.50	0.375	15	2.62	0.14	-0.80	-0.88	-0.97	-0.85
S20-0500-1000-15	20	4.08	0.50	1.00	0.750	15	2.81	0.14	-0.73	-0.77	-0.86	-0.79
S20-0500-2000-15	20	4.08	0.50	2.00	1.500	15	2.91	0.13	-0.71	-0.75	-0.83	-0.80
S20-0250-1000-15	20	4.08	0.25	1.00	0.375	15	1.94	0.14	-1.01	-1.08	-1.17	-0.70
S20-1000-0500-15	20	4.08	1.00	0.50	0.750	15	3.17	0.13	-0.64	-0.66	-0.72	-0.83
S20-1000-0250-15	20	4.08	1.00	0.25	0.375	15	2.87	0.14	-0.82	-0.94	-1.05	-0.90
S20-1000-1000-15	20	4.08	1.00	1.00	1.500	15	3.18	0.13	-0.65	-0.68	-0.76	-1.05
S20-1000-2000-15	20	4.08	1.00	2.00	3.000	15	3.25	0.13	-0.60	-0.64	-0.71	-1.05
S20-1000-4000-15	20	4.08	1.00	4.00	6.000	15	3.34	0.13	-0.61	-0.63	-0.70	-0.84
S20-2000-0500-15	20	4.08	2.00	0.50	1.500	15	3.48	0.13	-0.52	-0.51	-0.57	-0.76
S20-2000-1000-15	20	4.08	2.00	1.00	3.000	15	3.46	0.12	-0.50	-0.51	-0.59	-0.87
S20-2000-2000-15	20	4.08	2.00	2.00	6.000	15	3.55	0.11	-0.40	-0.38	-0.43	-0.82
S20-4000-1000-15	20	4.08	4.00	1.00	6.000	15	3.59	0.12	-0.34	-0.32	-0.37	-0.74
S20-4000-2000-15	20	4.08	4.00	2.00	12.000	15	3.56	0.12	-0.40	-0.40	-0.47	-0.79

Table 2. Same as Table 1 but for models using the 25 $M_\odot$ progenitor as the pre-collapse model.

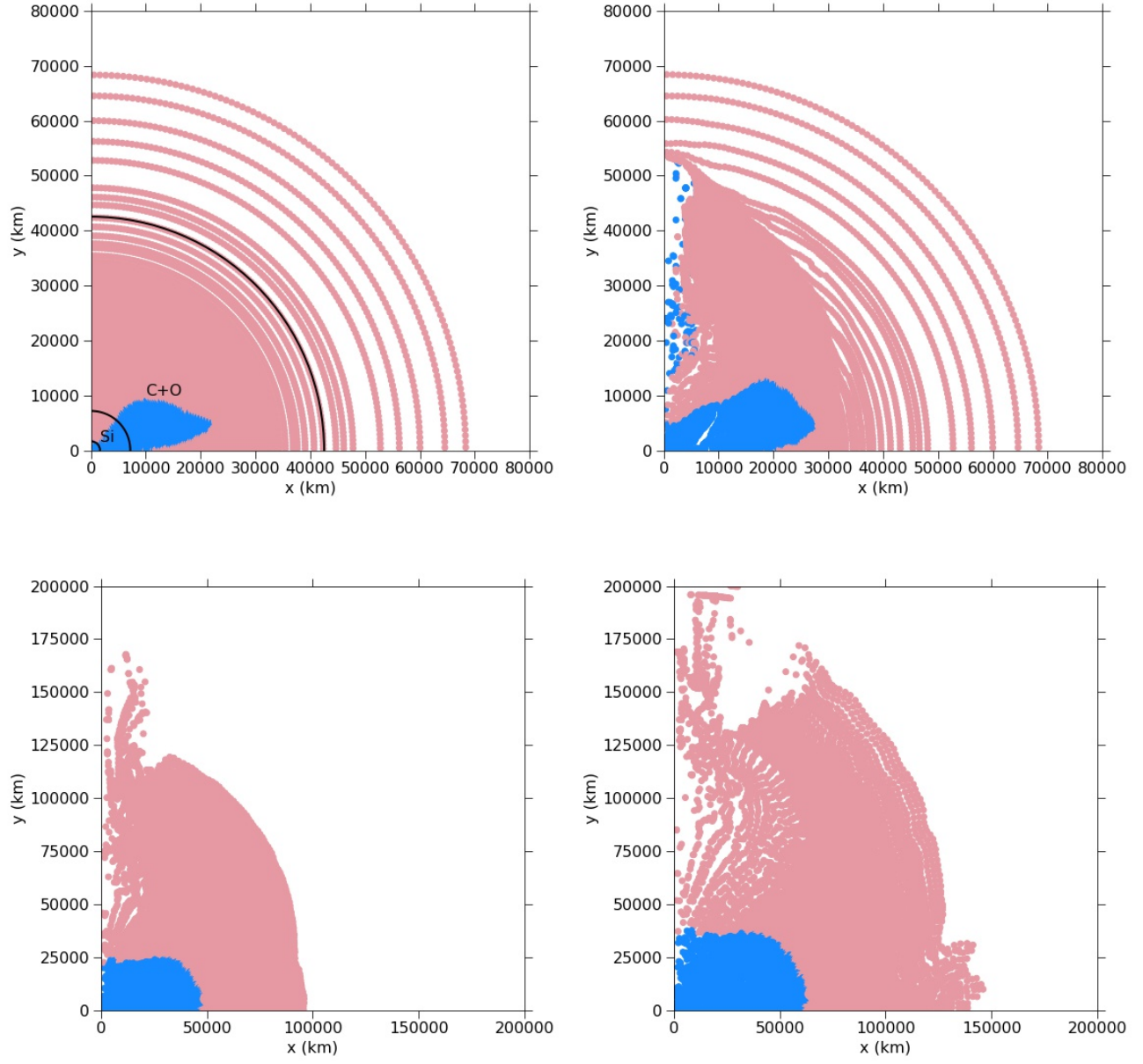| Model	$M_{\rm ZAMS}$	$M_{\rm pro}$	$\dot{E}_{\rm dep}$	$t_{\rm dep}$	$E_{\rm dep}$	$\theta_{\rm jet}$	$M_{\rm ej}$	[Ne/O]	[Si/O]	[S/O]	[Ar/O]	[Fe/O]
S25-0500-0500-15	25	5.58	0.50	0.50	0.375	15	2.62	-0.30	-0.33	-0.26	-0.35	-0.29
S25-0500-1000-15	25	5.58	0.50	1.00	0.750	15	2.74	-0.35	-0.14	-0.07	-0.13	-0.19
S25-0500-2000-15	25	5.58	0.50	2.00	1.500	15	2.50	-0.36	-0.20	-0.14	-0.20	-0.57
S25-0500-4000-15	25	5.58	0.50	4.00	3.000	15	3.02	-0.34	-0.14	-0.08	-0.15	-0.20
S25-0250-1000-15	25	5.58	0.25	1.00	0.375	15	1.76	-0.33	-0.11	-0.01	-0.06	-0.02
S25-0250-2000-15	25	5.58	0.25	2.00	0.750	15	1.51	-0.41	-0.06	0.02	-0.03	-0.89
S25-1000-0500-15	25	5.58	1.00	0.50	0.750	15	3.31	-0.31	-0.20	-0.16	-0.22	-0.31
S25-1000-0250-15	25	5.58	1.00	0.25	0.375	15	1.50	-0.33	-0.62	-0.60	-0.67	-0.41
S25-1000-1000-15	25	5.58	1.00	1.00	1.500	15	3.61	-0.33	-0.12	-0.08	-0.13	-0.20
S25-1000-1000-30	25	5.58	1.00	1.00	1.500	30	3.75	-0.37	-0.08	-0.05	-0.11	-0.11
S25-1000-2000-15	25	5.58	1.00	2.00	3.000	15	3.62	-0.32	-0.13	-0.09	-0.16	-0.19
S25-1000-2000-30	25	5.58	1.00	2.00	3.000	30	3.84	-0.37	-0.04	-0.01	-0.06	0.01
S25-1000-4000-15	25	5.58	1.00	4.00	6.000	15	3.20	-0.32	-0.26	-0.26	-0.34	-0.75
S25-2000-0500-15	25	5.58	2.00	0.50	1.500	15	3.97	-0.34	-0.12	-0.11	-0.17	-0.17
S25-2000-0250-15	25	5.58	2.00	0.25	0.750	15	3.63	-0.29	-0.27	-0.26	-0.32	-0.19
S25-2000-1000-15	25	5.58	2.00	1.00	3.000	15	4.00	-0.36	-0.11	-0.11	-0.18	-0.20
S25-2000-1000-30	25	5.58	2.00	1.00	3.000	30	4.12	-0.39	-0.03	-0.01	-0.07	-0.00
S25-2000-2000-15	25	5.58	2.00	2.00	6.000	15	4.02	-0.41	-0.08	-0.11	-0.19	-0.29
S25-2000-2000-30	25	5.58	2.00	2.00	6.000	30	4.23	-0.43	0.04	0.07	0.01	0.07
S25-4000-0500-15	25	5.58	4.00	0.50	3.000	15	4.33	-0.41	-0.01	-0.00	-0.06	-0.15
S25-4000-1000-15	25	5.58	4.00	1.00	6.000	15	4.29	-0.49	0.09	0.11	0.05	-0.19
S25-4000-2000-15	25	5.58	4.00	2.00	12.00	15	4.44	-0.36	-0.11	-0.15	-0.23	-0.14

Figure 1. The tracers distribution of the characteristic 25 $M_\odot$ model, with red being ejected and blue being bound. the Si and C+O cores are indicated by solid line for illustration. The top left, top right, bottom left and bottom right panels stand for four snapshots at equal time steps of ~ 4 s, starting from the initial profile.

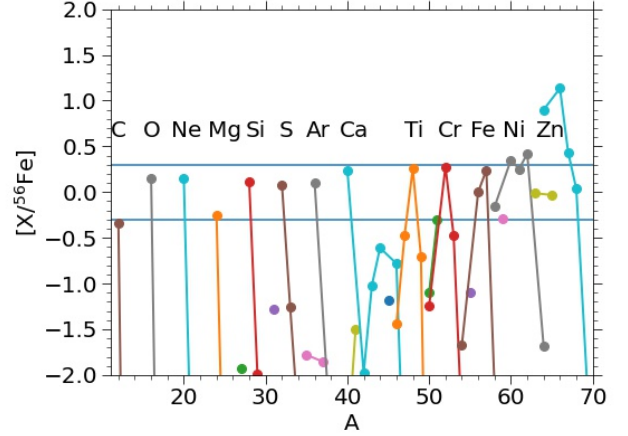**Table 3.** Same as Table 2 but with an innermost boundary at 1500 km.

Model	$M_{\rm ZAMS}$	$M_{\rm pro}$	$\dot{E}_{\rm dep}$	$t_{\rm dep}$	$E_{\rm dep}$	$\theta_{\rm jet}$	$M_{\rm ej}$	[Ne/O]	[Si/O]	[S/O]	[Ar/O]	[Fe/O]
S25b-0500-1000-15	25	5.34	0.50	1.00	0.750	15	1.55	-0.33	-0.13	-0.04	-0.10	-0.14
S25b-0500-2000-15	25	5.34	0.50	2.00	1.500	15	1.41	-0.37	-0.22	-0.12	-0.16	-0.67
S25b-1000-0500-15	25	5.34	1.00	0.50	0.750	15	2.06	-0.35	-0.22	-0.15	-0.20	-0.50
S25b-1000-1000-15	25	5.34	1.00	1.00	1.500	15	2.37	-0.34	-0.18	-0.12	-0.17	-0.29
S25b-1000-2000-15	25	5.34	1.00	2.00	3.000	15	2.46	-0.34	-0.15	-0.10	-0.16	-0.26
S25b-2000-0500-15	25	5.34	2.00	0.50	1.500	15	2.83	-0.33	-0.16	-0.13	-0.19	-0.30
S25b-2000-1000-15	25	5.34	2.00	1.00	3.000	15	2.91	-0.35	-0.12	-0.10	-0.16	-0.29
S25b-2000-2000-15	25	5.34	2.00	2.00	6.000	15	2.92	-0.36	-0.13	-0.14	-0.21	-0.28
S25b-1000-4000-15	25	5.34	1.00	4.00	6.000	15	2.48	-0.36	-0.24	-0.25	-0.33	-0.76
S25b-4000-1000-15	25	5.34	4.00	1.00	6.000	15	3.03	-0.40	-0.00	0.03	-0.03	-0.39
S25b-4000-2000-15	25	5.34	4.00	2.00	12.000	15	3.06	-0.47	0.10	0.14	0.08	-0.42

Table 4. Same as Table 2 but with an innermost boundary at 2100 km.

Model	$M_{\rm ZAMS}$	$M_{\rm pro}$	$\dot{E}_{\rm dep}$	$t_{\rm dep}$	$E_{\rm dep}$	$\theta_{\rm jet}$	$M_{\rm ej}$	[Ne/O]	[Si/O]	[S/O]	[Ar/O]	[Fe/O]
S25c-0500-1000-15	25	5.21	0.50	1.00	0.750	15	1.48	-0.29	-0.31	-0.25	-0.32	-0.13
S25c-0500-2000-15	25	5.21	0.50	2.00	1.500	15	2.00	-0.33	-0.14	-0.05	-0.12	-0.35
S25c-1000-0500-15	25	5.21	1.00	0.50	0.750	15	2.05	-0.34	-0.21	-0.13	-0.18	-0.23
S25c-1000-1000-15	25	5.21	1.00	1.00	1.500	15	2.34	-0.33	-0.21	-0.14	-0.20	-0.36
S25c-1000-2000-15	25	5.21	1.00	2.00	3.000	15	2.90	-0.34	-0.23	-0.19	-0.27	-0.59
S25c-2000-0500-15	25	5.21	2.00	0.50	1.500	15	3.15	-0.33	-0.19	-0.14	-0.21	-0.40
S25c-2000-1000-15	25	5.21	2.00	1.00	3.000	15	3.63	-0.32	-0.16	-0.12	-0.18	-0.45
S25c-2000-2000-15	25	5.21	2.00	2.00	6.000	15	4.00	-0.37	-0.08	-0.07	-0.15	-0.42
S25c-1000-4000-15	25	5.21	1.00	4.00	6.000	15	3.40	-0.35	-0.22	-0.21	-0.28	-0.74
S25c-4000-1000-15	25	5.21	4.00	1.00	6.000	15	3.83	-0.35	-0.12	-0.10	-0.16	-0.70
S25c-4000-2000-15	25	5.21	4.00	2.00	12.000	15	4.02	-0.43	0.01	0.02	-0.05	-0.48
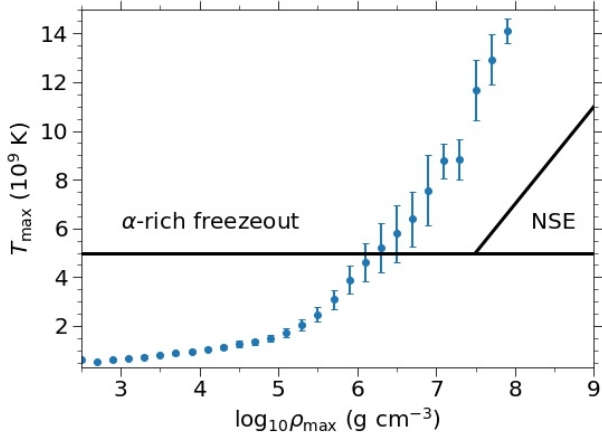
Figure 2. Statistics of the tracers for the peak temperature $T_{\rm max}$ and their corresponding density in the characteristic model S25-1000-1000-15.

Figure 3. The scaled isotope fraction ($[X/{\rm Fe}] = \log_{10}(X/{\rm Fe})/(X/{\rm Fe})_\odot$) for elements from C to Zn. The two horizontal lines stand for 50% and 200% of the solar value.

mass ejection by using the spherical explosion model (see the appendix of Tominaga et al. 2007b). The model con-

sidered the process that, instead of the ejection of the entire star, a part of the inner core and outer envelope

are mixed and ejected, and the remaining matter falls back and accreted onto the central compact object. The model assumes three parameters: (1) the inner mass-cut $M_{\rm cut,\ in}$, (2) the outer mass-cut $M_{\rm cut,\ out}$ and (3) the mixing ratio $f_{\rm mix}$. The mass interior to the inner mass-cut all accretes. The total accreted mass is given by

$$M_{\rm acc} = M_{\rm cut,in} + (1 - f_{\rm mix})(M_{\rm cut,out} - M_{\rm cut,in}) \quad (2)$$

The exact mass of individual elements then depends on both the composition of the middle layer and the outer layer. This model has been used extensively to describe the origin of the peculiar chemical abundance patterns in extremely metal-poor stars (e.g., Iwamoto et al. 2005; Ishigaki et al. 2018).

The mixing-fallback model can reproduce the abundance pattern of jet-like explosion rather well Tominaga (2009). However, the spherical model is different from a full 2- or 3D models. Assuming the explosion of the same energy, the energy is deposited in a spherical shell, rather than being focused on the cone shaped structure. Thus, the mixing-fallback model has (1) a less active nucleosynthesis and (2) a lower ejecta velocity.

3. EXPLOSIVE OBSERVABLE AND NUCLEOSYNTHESIS

3.1. *Dependence on Dimensionality*

The most important effect of the jet-driven explosion on supernova models is that the jet provides local heating for the matter to expand and to be ejected. This cannot be achieved in classical spherical models. In the aspherical model compared with the spherical model, a small explosion energy is enough for the ejecta to reach such high velocities as observed in some hypernovae or highly aspherical supernovae (e.g., SN 1998bw studied in Nakamura et al. 2001; Höflich et al. 1999; Mazzali et al. 2001). This allows the aspherical model to synthesize and eject Fe-group elements more readily than the spherical model with the same explosion energy. Here we examine how the dimensionality changes nucleosynthetic products.

In Figure 4 we plot the tracer thermodynamics for the jet-driven supernova model using the 25 $M_\odot$ star as the progenitor, and compare with the spherical explosion model. The difference in the heating history is clear on the tracer particles. (1) In the 1D model, there are large variations in the temperature in the inner core with $\rho_{\rm max} > 10^7$ g cm^{-3}. However, there are very small or even no variations for tracers below that density. This is because the shock in the spherical model has lost most of its compressional heating effect at $\rho_{\rm max} < 10^7$ g cm^{-3}. (2) On the other hand, the angular effects remain clear
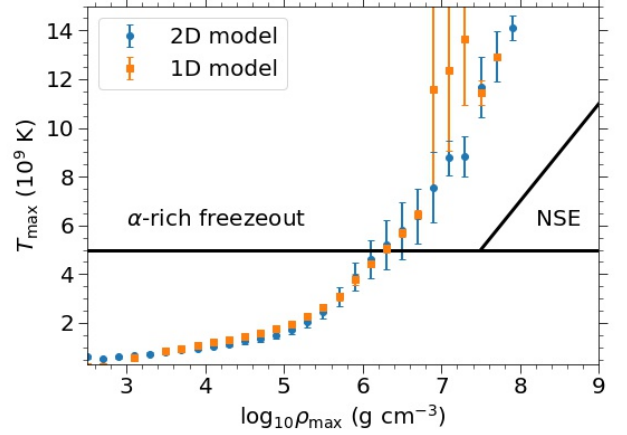
Figure 4. The tracer thermodynamics history for the 25 $M_\odot$ star assuming spherical (1D: orange squares) and jet-powered (2D: blue circles) explosions.

to be seen for the 2D model down to 10^5 g cm^{-3}. This suggests that the energy confined within 15–30° helps the shock to maintain its strength to a larger spatial extension.

In Figure 5 we plot the abundance patterns of our characteristic models using 20, 25 and 40 $M_\odot$ progenitors, in comparison with the corresponding spherical (1D) models. Both sequences of models assume the same explosion energy $\sim 1.5 \times 10^{51}$ erg.

The progenitor mass also affects how the 2D and 1D models differ from each other. For the lower mass model (20 $M_\odot$), the 2D explosion leads to the prominent overproduction of O- and Si-group elements along the α-chain, ^{16}O, ^{20}Ne and ^{24}Mg. This can be understood by the entire ejection of the outer layers. The odd-number Si-group elements are underproduced in both models, with the exception that Ti and Cr are well-produced in 1D models. The Fe-group elements in both models are similar to the solar ratio, while Ni is significantly overproduced in the 1D model. Zn is also overproduced in the 1D model but is substantially underproduced in the 2D model.

The 25 $M_\odot$ model is like a mixture of the 20 and 40 $M_\odot$ models. The O-group elements are weaker for the 1D model while the Si-group elements are stronger. The chemical abundances from Si to Fe are very close to the solar abundances in both dimensionalities, with the exception of the odd-number elements. Ni is again overproduced in the spherical model. The overproduction suggests that, to reconcile with the solar abundance, the ejecta cannot contain the entire inner core of the star. The overproduction is less severe in the 2D model.

The 40 $M_\odot$ is in sharp contrast with the 20 $M_\odot$ model. Most α-chain elements from Ne to Ti in the 2D model are underproduced while the 1D model produces the amounts close to the solar values. The 2D model contains more weights in the Fe-group elements. The ejecta in the 2D model contains a clear Zn signature but a very low Ni abundance, which is an opposite in the 1D counterpart.

To further visualize the effect of the mixing in one-dimension and the two-dimensional jet-driven explosions, we show in Figure 6 the one-dimensional spherical model yields using the mixing-fallback mechanism, and in Figure 7 the two-dimensional model sequences. In all 1D models, we choose the $E_\mathrm{exp} = 1 \times 10^{52}$ erg as the reference and vary the mixing parameter from $0 - 0.3$ in 0.05 steps. This corresponds to the jet angle $\sim 45°$. Different mixing masses are used from $3.0 - 6.0$ $M_\odot$ for each model. We focus on the element pairs [Ne/O], [Ar/O] and [S/O] against [Fe/O] as these elements are frequently observed in galaxies.

The one-dimensional spherical models in Figure 6 show vertical variations for different mixing ratios. We note: (1) [Ne/O] in one-dimensional models is a good indicator of the progenitor mass because of the following reason. Ne is synthesized by C-burning which produces larger $X(\mathrm{Ne})$ from larger $X(\mathrm{C})$ in the C+O core. The C/O ratio is smaller for the larger $^{12}\mathrm{C}(\alpha, \gamma)^{16}\mathrm{O}$ reaction rate which is higher for higher temperatures. Since the temperature in the C+O core is higher for the larger progenitor mass, the C/O ratio and thus the Ne/O ratio are smaller for a larger progenitor mass. The ratio does not depend on the mixing level or the mass cut.

(2) The [Fe/O] of all spherical models are sub-solar because the massive C+O-layer is ejected, which strongly suppresses the ratio. This is in contrast to the 2D model, where a significant fraction of the O-layer is accreted rather than ejected (see Figure 1). The sub-solar patterns persist among all masses.

(3) For [Ar/O] and [S/O], there are two groups of models. When the mass cut is deep enough to completely isolate the Si-core, these ratios against [Fe/O] appear to be slightly supersolar and vertical (right side of the plot). When the mass cut is moved outward, the ratios appear to align on a straight line. This is because the inner core also contains Ar and S.

The two-dimensional models in Figure 7 show qualitatively different patterns from their one-dimensional models except [Ne/O].

(1) [Ne/O] against [Fe/O] preserves its strong mass-dependence as in the 1D models.

(2) Other two element pairs show a large scatter. The [Fe/O] ratio is significantly higher than most 1D models.
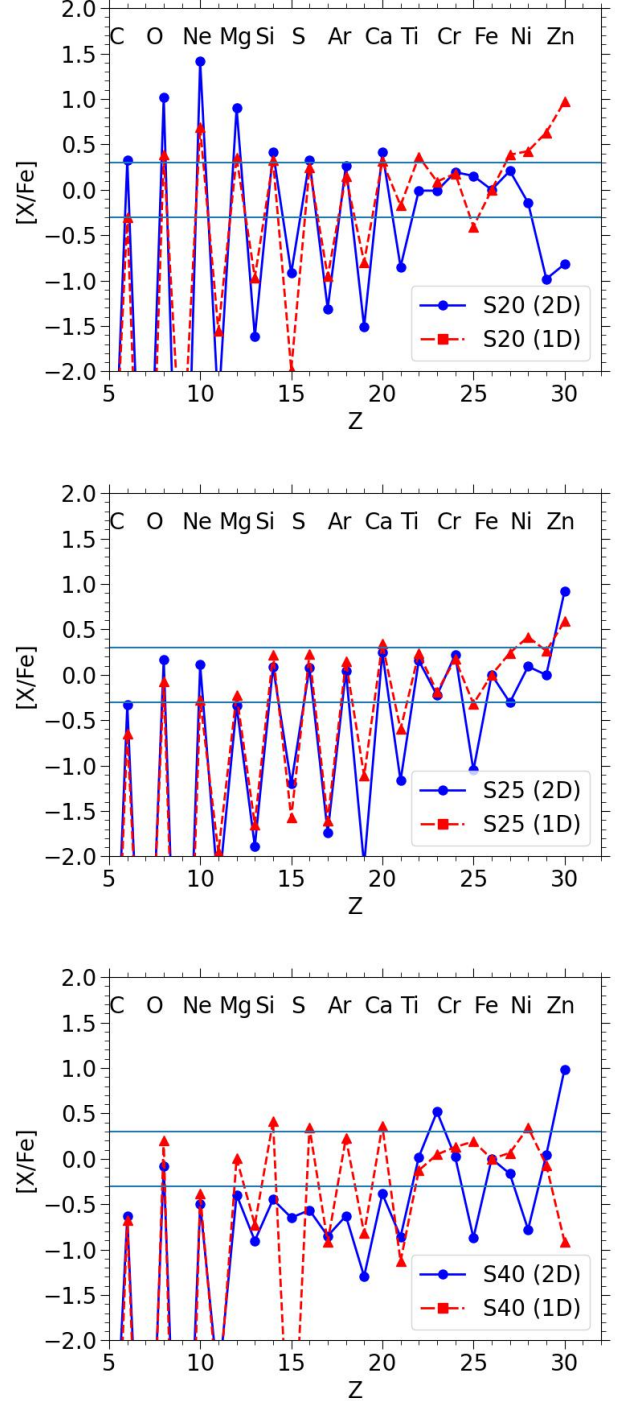
Figure 5. (top panel) The chemical abundances of Models S20-1000-1000-15 (blue solid line) and its one-dimensional counterpart (red dashed line). (middle panel) Same as the top panel but for Models S25-1000-1000-15 and its 1D counterpart. (bottom panel) Same as the top panel but for Models S40-1000-1000-15 and its 1D counterpart.

The 25 and 40 $M_\odot$ stars have much higher [Fe/O] than most one-dimensional counterpart.

(3) The 20 $M_\odot$ star shows distinctively lower [Fe/O], [Ar/O] and [S/O] than more massive stars, because its more compact progenitor leads to very strong fallback of the Si core as we show in the next section. Such fallback suppresses the synthesis and ejection of Fe. We also observe that [Ar/O] and [S/O] are very similar to each other. The distinction of the one-dimensional approximation and two-dimensional models further indicates the needs of the self-consistent simulations for correctly predicting the mixing and fallback process.

3.2. *Dependence on Progenitor Mass*

In Figure 8 we present the distribution of the tracer particles for the 20 $M_\odot$ model using the standard jet energetics. The progenitor has thin Si and C+O layers at the onset of collapse. Despite this model has a lower binding energy than the 25 $M_\odot$ model counterpart, a larger fraction of the Si layer remains bound at the end of simulation. We note that both models receive the same amount of the deposited energy. The inner C+O layer is ejected in an aspherical manner. The cone shaped ejecta, with the energy deposition being confined within 15°, can extend beyond 45°. Matter above $\sim 15,000$ km is fully ejected.

Similar to the above plot, we plot the tracers for the 40 $M_\odot$ model in Figure 9. The tracers which can escape show a clearer jet structure. It can be separated into two parts. Below $r \sim 30,000$ km, the tracers are limited to the cone similar to the jet, but with a wider open angle $\sim 30°$. Above 30,000 km, ejecta appears to be spherical in distribution, with the exception near the boundary.

In Figure 10 we show a plot of tracers being similar to Figure 2 but including models with different progenitor masses. All three models show monotonically increasing distributions of $T_{\max}$ against $\rho_{\max}$, suggesting that the shock is propagating only outward radially, without observable reflection or collision. The 25 and 40 $M_\odot$ models are less compact than the 20 $M_\odot$ model but show similar tracer distributions. The temperature fluctuations at $\rho = 10^5 - 10^7$ g cm^{-3} are smaller for 25 and 40 $M_\odot$ models than 20 $M_\odot$. All models show that at $\rho > 10^6$ g cm^{-3} the tracers experience only α-rich freezeout.

In Figure 11, we plot the mass fraction of the ejecta. The ejecta mass fraction is the mass fraction of passive tracer particles which have a positive total energy by the end of the simulation. These tracers, which are also post-processed for nucleosynthesis, are the matter to be ejected in the explosion. For each progenitor mass, the ejecta fraction tends to increase as the deposited energy
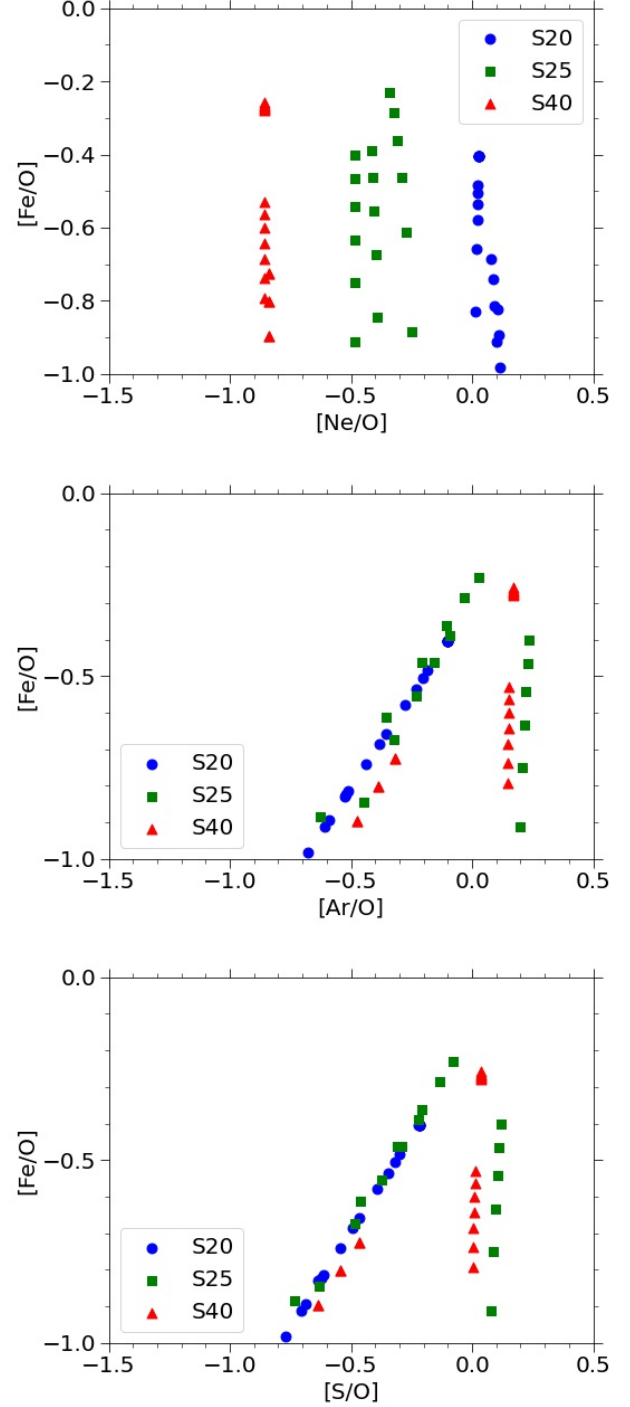
Figure 6. The nucleosynthetic yields of the one-dimensional spherical explosion models with the mixing-fallback mechanism to approximate the aspherical yields. Mixing masses of $3 - 6 M_\odot$ are adopted. (top panel) [Fe/O] against [Ne/O]. (middle panel) [Fe/O] against [Ar/O]. (bottom panel) [Fe/O] against [S/O].
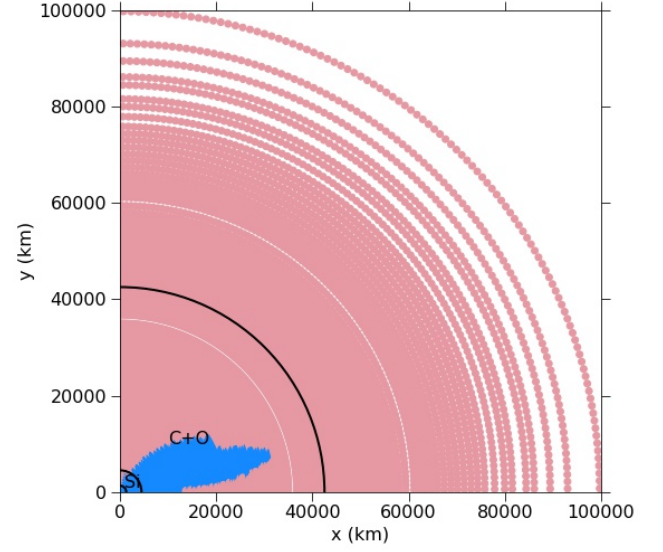
Figure 8. Same as Figure 1 but for the characteristic model of 20 $M_\odot$ as the progenitor.

Figure 7. Same as Figure 6 but for the 2D jet-driven supernova models presented in this work. (top panel) [Fe/O] against [Ne/O]. (middle panel) [Fe/O] against [Ar/O]. (bottom panel) [Fe/O] against [S/O].
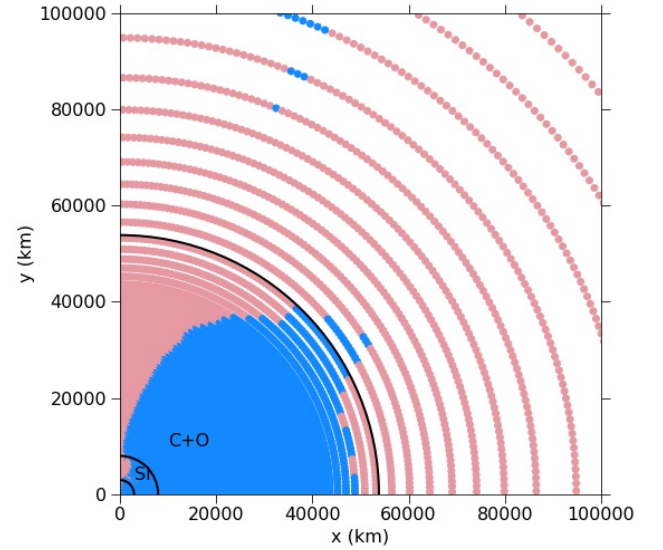
Figure 9. Similar to Figure 1 but for the characteristic model of 40 $M_\odot$ as the progenitor.

increases. There are large variations among models with the same deposited energy because the robustness of the ejection depends the shock strength, which consequently depends on the jet properties.

The ejecta mass fraction of the S20-series reaches the asymptotic value of ~ 0.85 at a relatively low deposited
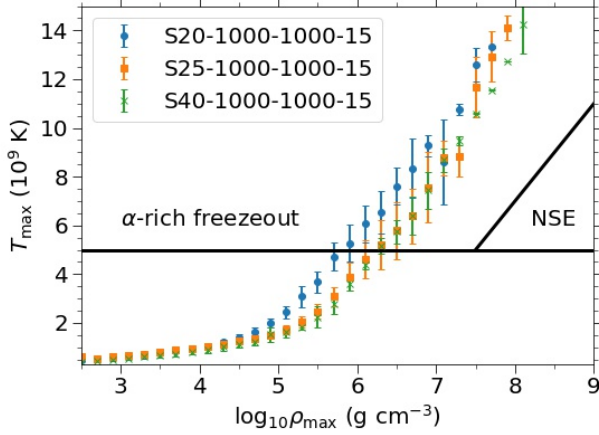
Figure 10. Same as Figure 2 but for the 20 $M_\odot$ and 40 $M_\odot$ progenitor models with the standard jet.
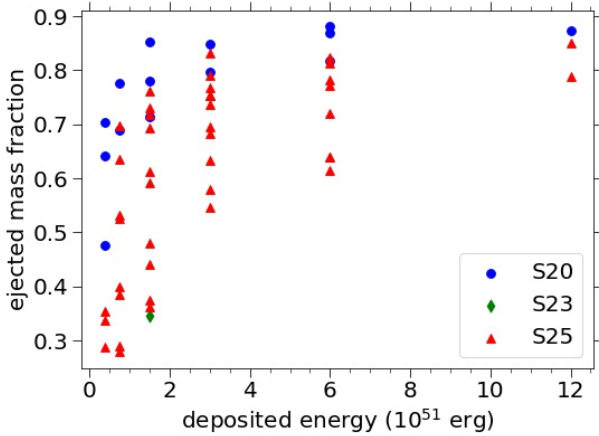
Figure 11. The ejecta mass fraction of the models in Tables 1 and 2

energy of $\sim 2 \times 10^{51}$ erg. On the other hand, the more massive progenitor of S25-series requires a higher deposited energy of $\sim 3 \times 10^{51}$ erg for the ejecta mass fraction to reach the asymptotic value of ~ 0.80. The lower asymptotic value can be understood because the more massive Si-core tends to be accreted regardless of the deposited energy. We remind that due to the jet geometry, the equatorial matter in the Si-core is less likely to be ejected.

In Figure 12 we plot the isotopic abundances of two contrasting models S20-1000-1000-15 (20 $M_\odot$) and S40-1000-1000-15 (40 $M_\odot$). The two models share the same jet energy but different progenitor masses. The differences of the pre-collapse structure in terms of the relative mass fractions of the C+O and Si-layers, together
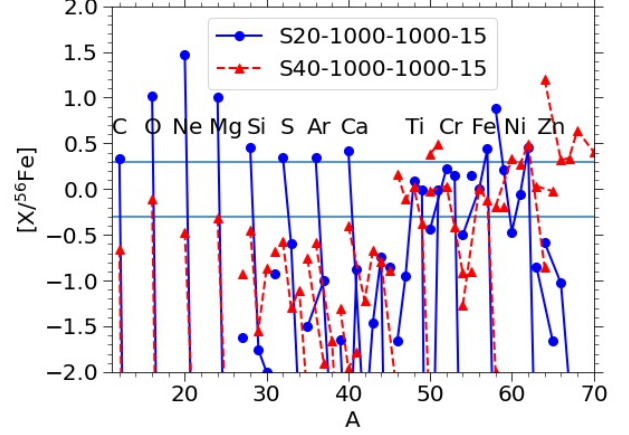
Figure 12. Chemical abundance patterns of Models S20-1000-1000-15 (20 $M_\odot$: blue solid line) and S40-1000-1000-15 (40 $M_\odot$: red dashed line).

with their binding energies, lead to very substantial differences in the abundance patterns.

The lower mass progenitor (20 $M_\odot$) produces such large ratios of O-group and Si-group isotopes relative to ^{56}Fe as $[(^{16}\mathrm{O},^{20}\mathrm{Ne},^{24}\mathrm{Mg})/^{56}\mathrm{Fe}] \gtrsim 1.0$, $[(^{28}\mathrm{Si},^{32}\mathrm{S},^{36}\mathrm{Ar},^{40}\mathrm{Ca})/^{56}\mathrm{Fe}] \gtrsim 0.3$ (and thus $[(^{16}\mathrm{O}/^{24}\mathrm{Si}] \gtrsim 0.2$).

In contrast, the higher mass progenitor (40 $M_\odot$) produces much smaller ratios of O-group and Si-group isotopes relative to ^{56}Fe, i.e., $[(^{16}\mathrm{O},^{20}\mathrm{Ne},^{24}\mathrm{Mg})/^{56}\mathrm{Fe}] \lesssim -0.1$, $[(^{28}\mathrm{Si},^{32}\mathrm{S},^{36}\mathrm{Ar},^{40}\mathrm{Ca})/^{56}\mathrm{Fe}] \lesssim -0.4$ (and thus $[(^{16}\mathrm{O}/^{24}\mathrm{Si}] \gtrsim 0.3$).

For Fe-group isotopes, the differences are irregular. For example, the lower mass model shows a suppressed ^{64}Zn production but an enhanced ^{58}Ni production relative to ^{56}Fe. In contrast, the higher mass model shows opposite ratios. Such a difference is due to the difference in the Y_e distribution.

3.3. *Effects of Mass Cut*

In Figures 13 and 14, we plot the tracer particle distribution for the 25 $M_\odot$ star being similar to Figure 1 but with the different mass cut (i.e., inner boundary) at radii of $R_{\mathrm{cut}} = 1500$ km and 2100 km, respectively. A direct comparison with Figure 1 shows a drastic difference in the ejecta mass and structure. While the two models have the same jet energy, the mass cut at the larger R_{cut} leads to more significant fallback including both the Si-core and the inner C+O-core. The ejection of the He-envelope is only mildly reduced.

The change of the mass cut to larger R_{cut} causes the following changes in the ejecta structure.

First, the mass cut at larger R_{cut} means the formation of a more massive compact object. Second, the larger

Figure 13. Similar to Figure 8 but for the mass cut at $R_{cut} = 1500$ km in the 25 $M_\odot$ model with the same jet parameters.
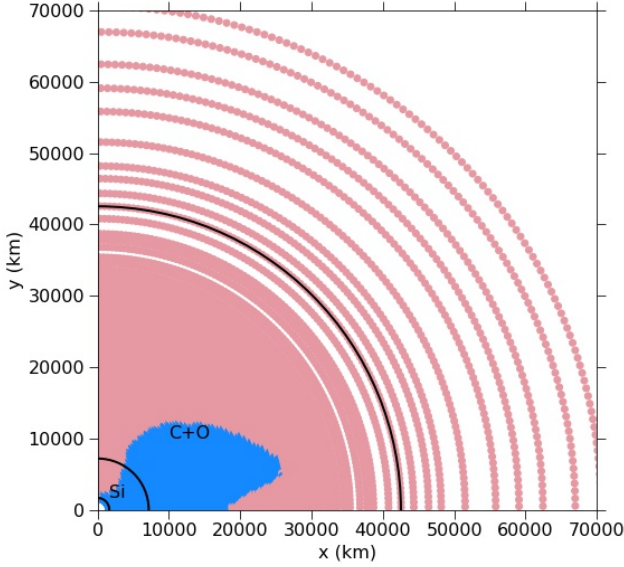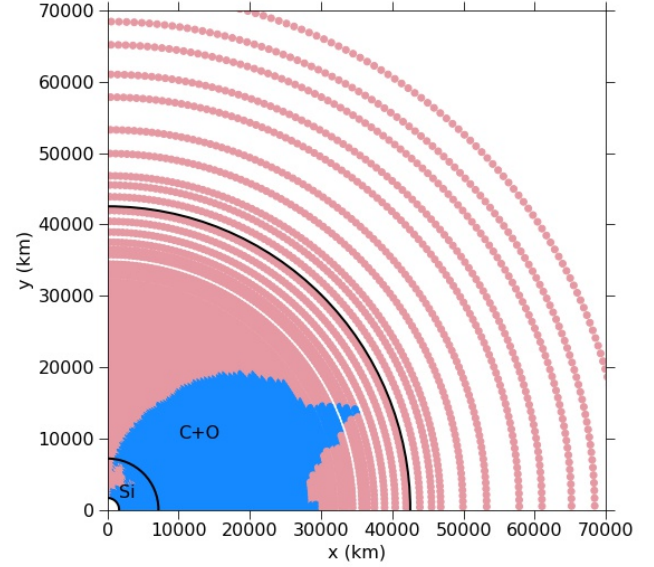

Figure 14. Similar to Figure 8 but for the mass cut at $R_{cut} = 2100$ km in the 25 $M_\odot$ model with the same jet parameters.

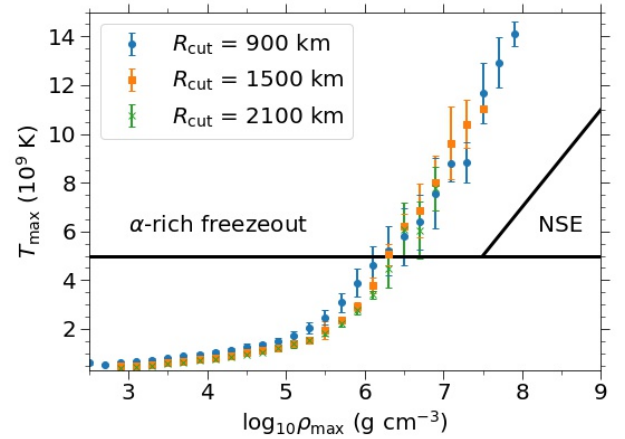R_{cut} leads to more mass receiving the jet energy. The final energy per unit mass after the jet deposition is lower, which means a weaker outgoing shock. The effect of $R_{cut} = 2100$ km is significant. Even with the same amount of deposited energy, the majority of the inner core fails to be ejected. Only the outskirt of the C+O core is ejected at the end of simulation.

In Figure 15 we show the thermodynamics history of our characteristic models using the 25 $M_\odot$ progenitor, but with the innermost radius of 900, 1500 and 2100 km, respectively. The maximum density experienced by the tracers is smaller for the larger inner radius. For the model with $R_{cut} = 2100$ km, all tracers have densities less than 10^7 g cm^{-3}.

In Figure 16, we compare the abundance patterns with different mass cuts. It does not show qualitative differences. The two models follow each other, with the model with a more extended mass cut (1500 km) have in general 20 – 50% higher in O-group and Si-group elements up to Ca. The relation flips for more massive elements. One exception is ^{50}Cr and ^{54}Cr. The more extended mass cut can boost its production. The mild difference of the Fe-group elements, mostly from the innermost region of the star, is small in terms of the mass cut. This agrees with the ejecta distribution that the narrow segment in the Si-core is ejected in both models. Also, the accreted matter is mostly C+O-rich matter which does not bring major nucleosynthetic changes to other elemental abundances.

Figure 15. The tracer thermodynamics history of the characteristic model using the 25 $M_\odot$ star as the progenitor with $R_{cut} = 900$, 1500 and 2100 km at the mass cut.

4. DISCUSSION

4.1. The Ti-V relation Revisited

Sneden et al. (2016) have found that [Ti/Fe] and [V/Fe] show a correlation of 45° based on the metal-poor stars catalogue derived in Roederer et al. (2014) (Fig. 17). In Leung et al. (2023), we have explored the [Ti/Fe] − [V/Fe] relation using the 40 $M_\odot$ models and compared with the observed relation. In our previous
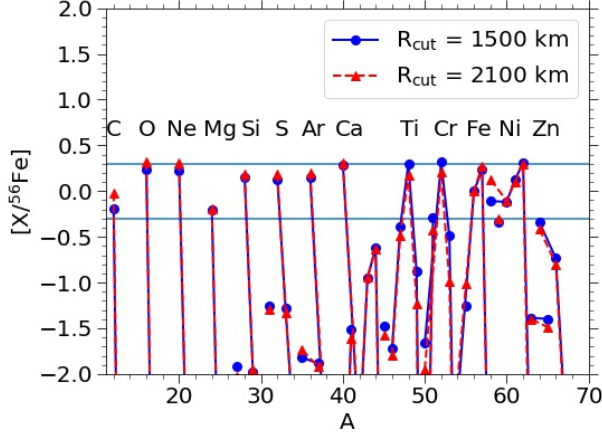
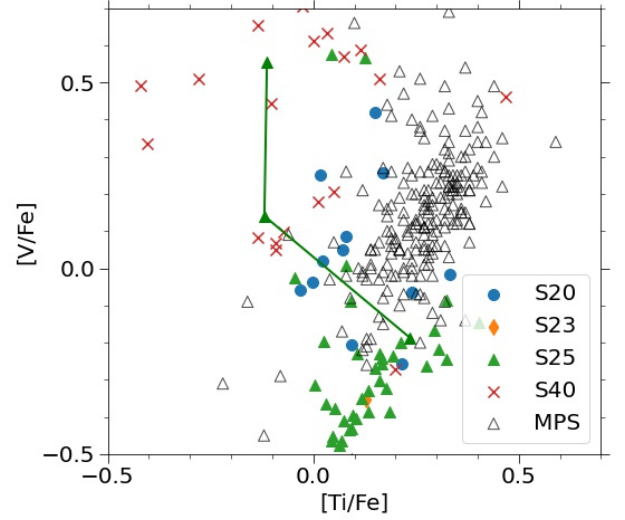**Figure 16.** The chemical abundance patterns of Model S25-1000-1000 with $R_{cut} = 1500$ km (blue solid line) and $R_{cut} = 2100$ km (red dashed line).

Figure 17. The [V/Fe] against [Ti/Fe] relation for the jet-driven supernova models in this work. The semi-transparent purple diamonds stand for the metal-poor star data taken from (Roederer et al. 2014). The straight line connects the spherical explosion models of S25 with different explosion energies.

work, the 45° relation is reproduced but the interception differs from the data.

In Figure 17, we extend our comparison with the available data by including our new models. Being consistent with our 40 $M_\odot$ models, there is also a clear trend in our 25 $M_\odot$ models which also show a 45° inclination in the [Ti/Fe]–[V/Fe] plane. The 20 $M_\odot$ series of models, on the contrary, does not show a clear trend but their composition is closer to the cluster formed by the observational data. The 40 $M_\odot$ models are in general very remote to those EMP stars. They have a much higher [V/Fe] ratio.

To compare with the spherical explosion models, we also show one particular mass of 25 $M_\odot$ with different explosion energy. It shows that in the high energy limit, the spherical model resembles with our aspherical models. This agrees with our expectation that the jet model can create high-entropy matter which is similar to a very strong explosion in the spherical case.

If we extend the data assuming a linear trend, the intercepts of models with different progenitor mass does not vary monotonically. It is because in the lower mass models, the fallback becomes important that the Fe production is also affected. It suggests a non-linear competition between lowering the mass and the enhanced production of [Ti/Fe]. A further inspection will be useful for exploring the mass dependence of this element pair.

4.2. ^{56}Ni mass and ejecta mass relation

An interesting relation for Type Ib/c supernovae is the correlation between the ejected ^{56}Ni mass (M_{56}) against the ejecta mass (M_{ej}). These two quantities can be well extracted from the light curve. Qualitatively, the peak brightness and the width of the light curve determines

the M_{56} and M_{ej}, respectively. In the iPTF (Intermediate Palomar Transient Factory) surveys presented in De Cia et al. (2018); Gomez et al. (2022); Taddia et al. (2019), a clustering is observed for this kind of supernovae. Here we examine if a similar relation can be reproduced for the jet-driven models.

In Figure 18, we plot M_{56}–M_{ej} relation for the catalog in this work and the surveys described above. It shows that models with different progenitor masses have significant overlap in the parameter space as follows. (1) The S20 series does not exhibit large variations and it is suitable to explain the faint supernovae of $M_{56} < 0.1\ M_\odot$ with $M_{ej} = 0.1 - 0.5\ M_\odot$. (2) The S40 series has a clear rising trend of M_{56}. (3) The S25 series has M_{56} less sensitive to M_{ej}. The contrast among these series is related to the compactness of the progenitor model. In a lower mass model, the higher compactness leads to strong fallback in the inner core.

By observing how the theoretical data overlap with the observational data, we conclude that the 25 $M_\odot$ series agrees with the observed Type Ib/c supernovae from Taddia et al. (2019) and Gomez et al. (2022). These supernovae (including the well observed SN 1998bw and 2006aj) have typically $M_{56} \sim 0.1 - 1\ M_\odot$ and $M_{ej} = 1 - 10\ M_\odot$. However, the jet-driven supernova cannot explain directly the data point with a $M_{ej} > 0.5\ M_\odot$ and a low M_{56} ($< 0.1\ M_\odot$). Similarly, this model cannot fully explain supernovae with high M_{56} ($> 1\ M_\odot$).
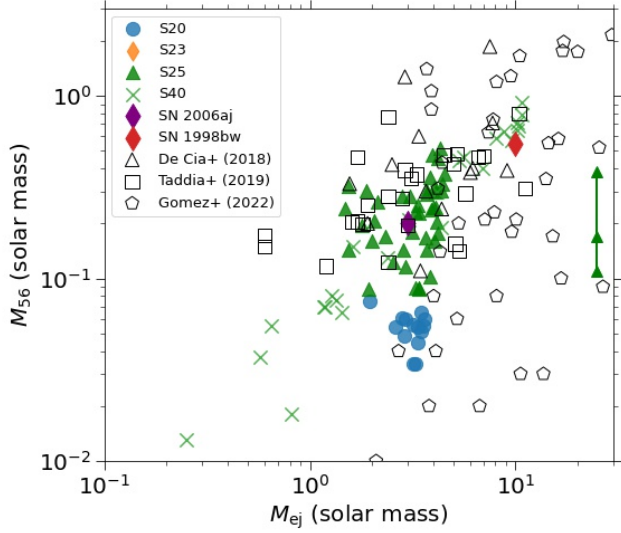
Figure 18. The ejected ^{56}Ni mass (M_{56}) against the ejecta mass (M_{ej}) of the jet-driven supernova models in this work (20 $M_\odot$ series: blue circles, 25 $M_\odot$-series: orange diamonds, and 40 $M_\odot$-series: green crosses). The plot is overlaid with the observed Type Ib/c supernova catalog taken from De Cia et al. (2018) (brown triangles), Taddia et al. (2019) (pink squares), Gomez et al. (2022) (grey pentagons). The green triangles connected with the line are the spherical explosions of the S25 models with different explosion energies.

We also include the spherical explosion model for the S25 progenitor shown the triangles with a line. The high explosion energy makes the entire envelope ejected. Thus, M_{ej} does not change significantly across different explosion energy. M_{56} increases sharply as the explosion energy increases. The high M_{ej} does not well resemble to the clustering of the data.

4.3. *Elemental Abundance of Jet-Driven Supernovae*

In the previous sections, we have presented the detailed isotopic abundances of our models. In this section, we compare our results with some well-observed metal-poor galaxies. These galaxies, some of these having relatively low metallicity, are good test cases for our zero metallicity models because such early galaxies might have a much lower fraction of metal enrichment by Type Ia supernovae. Most explosions are contributed by either spherical and aspherical massive star explosions. Therefore, it reduces the dependence on some of the uncertain parameters in Type Ia supernovae, such as the explosion channel (Leung & Nomoto 2023) and the delay time (Kobayashi et al. 2020).

In Figure 19 we aggregate the abundances element-wise and plot the elemental abundance patterns. The graph provides a direct comparison with observational data because the spectral lines from galaxies do not dis-
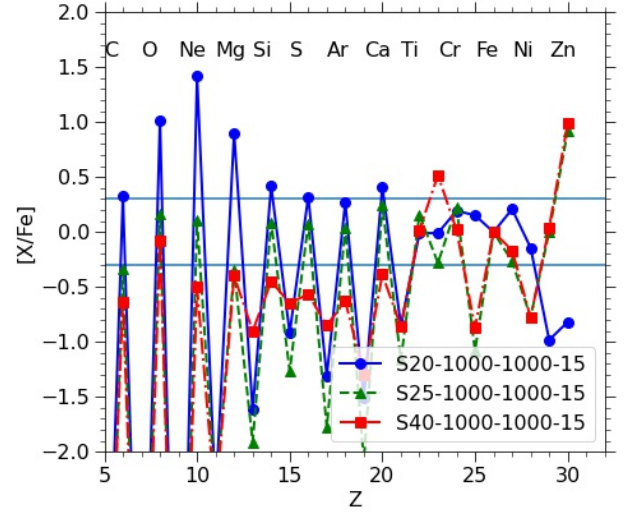
Figure 19. The elemental abundances [X/Fe] of our characteristic models using 20 $M_\odot$ (blue solid line, circle), 25 $M_\odot$ (green dashed line, triangle) and 40 $M_\odot$ (red dot-dashed line, square) models. The two lines correspond to 50% and 200% of the solar value.

tinguish the detailed distribution across stable isotopes. Nonetheless, we stress that the isotopic distribution is equally important because it allows us to clarify the explosion physics quantitatively.

Figure 19 shows that [(C-Ca)/Fe] > 0.3 in the 20 $M_\odot$ model, while [(C-Ca)/Fe] < −0.1 in the 40 $M_\odot$ model. The 25 $M_\odot$ model has the chemical abundance most proximate to the solar abundance pattern. All three models show a comparable Fe-group element production, with the exception near Zn. The higher mass model tends to produce more Zn than the lower mass models.

5. COMPARISON WITH OBSERVATIONAL DATA

5.1. *Extremely Metal Poor Galaxies*

In Watanabe et al. (2023) the EMPRESS survey continues to analyze the chemical abundances of some metal-poor galaxies. The analysis includes two new objects SBS-0335-052E and J0125+0759. In Table 5 we list the abundance data of these galaxies, together with some other metal-poor galaxies collected from relevant surveys. Similar to Mao et al. (2021), Ne, Ar, S and Fe relative to O are measured. We list the galaxies we have used for our comparison in Table 5.

Table 6 lists the EMPG studied in this work. We focus on the samples which have good measurements of the Ne/O and Ar/O ratios. Among these EMPGs, they share similar values of $\log_{10}$ Ar/O $\sim$ −2.3, which is significantly sub-solar. Their Ne/O ratio $\log_{10}$ Ne/O $\sim$ −0.6 is slightly sub-solar. The relatively flat distribution of the Ar/O ratio among these galaxies sug-

Table 5. The chemical abundance data of some extremely metal-poor galaxies collected from recent works as reported in Watanabe et al. (2023).

Galaxy ID	[Ne/O]	[S/O]	[Ar/O]	[Fe/O]	Reference
SBS-0335-052E	-0.27 ± 0.00	$0.018^{+0.05}_{-0.018}$	$-0.037^{+0.02}_{-0.03}$	$-0.24^{+0.11}_{-0.24}$	Watanabe et al. (2023)
J0125+0759	-0.01 ± 0.00	-0.34 ± 0.05	$-0.08^{+0.01}_{-0.08}$	$-0.24^{+0.12}_{-0.24}$	Watanabe et al. (2023)
J0159-0622	$-0.12^{+0.01}_{-0.02}$	-0.016 ± 0.06	-0.01 ± 0.02	$-0.51^{+0.17}_{-0.28}$	Isobe et al. (2022)
J1608+4337	0.107 ± 0.02	-0.07 ± 0.02	$-0.04^{+0.02}_{-0.03}$	$-0.43^{+0.15}_{-0.22}$	Isobe et al. (2022)
J2115-1734	$0.003^{+0.004}_{-0.005}$	-0.079 ± 0.06	$0.04^{+0.01}_{-0.06}$	$-0.41^{+0.03}_{-0.02}$	Kojima et al. (2020)
J0811+4730	-0.0048 ± 0.031	-0.117 ± 0.056	-0.245 ± 0.104	0.17 ± 0.092	Izotov et al. (2018)

Table 6. Elemental abundance data of EMPGs used in this work, as extracted in Isobe et al. (2022).

EMPG	$\log_{10}(\mathrm{Ne/O})$	$\log_{10}(\mathrm{Ar/O})$	$\log_{10}(\mathrm{Fe/O})$
J0156-0421	-0.759	-2.39	< -0.45
J0159-0622	-0.878	-2.32	-1.74
J0210-0124	-0.688	-2.37	-1.75
J0226-0517	-0.664	-2.38	-1.27
J0232-0248	-0.692	-2.42	-1.26

gest that these galaxies have experienced similar metal-enrichment history.

We should note that, for abundance comparisons between EMPGs and theoreical models, we need chemical evolution models of galaxies as mentioned in Watanabe et al. (2023). In the present work, we make a simple comparison between the $\sim 20 - 40\ M_\odot$ Pop III stars and EMPGs in order to study how important the jet-like explosions are for chemically enriching EMPGs. Also, $\sim 20-25\ M_\odot$ stars have been shown to make the largest contribution in chemical evolution of galaxies (Weaver et al. 1978; Woosley & Weaver 1995).

In Figure 20 we compare the post-explosion nucleosynthesis of our spherical models from $20 - 40\ M_\odot$ for different explosion energies. We demonstrate the mismatch between the "spherical" explosion models and EMPGs. We note that the smaller mass star tends to produce larger [Ne/O] with a weak dependence on the explosion energy. And the higher energy explosion produces smaller [Ar/O].

The progenitor mass dependence of [Ne/O] stems from the C/O ratio after He burning which is smaller for a larger mass because of the higher temperature during He burning. The trend of [Ar/O] is expected because a higher explosion energy implies a stronger shock and a higher post-shock temperature, which burn more O into Si, S, and Ar. This facilitates the fusion of the C+O core into elements beyond Ar. Among all models, only the models $\sim 20 - 30\ M_\odot$ have [Ne/O] close enough to the observational data. However, their [Ar/O] is too high
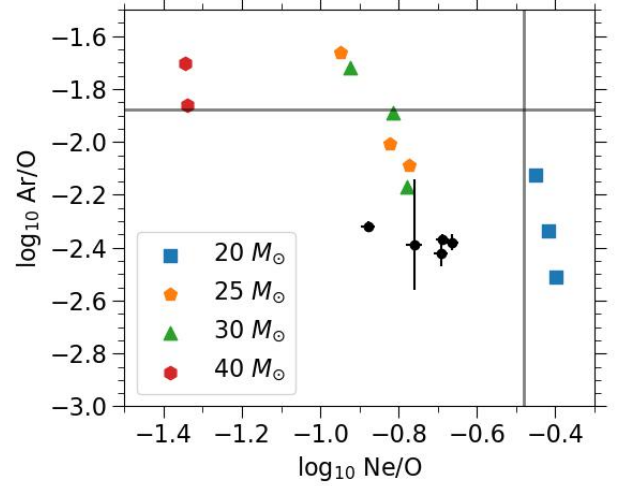
Figure 20. The comparison of the post-explosion [Ne/O] against [Ar/O] for selected EMPGs and the "spherical" explosion models. The straight line stands for the solar values of the corresponding isotope ratios. The data points correspond to the EMPGs reported in Isobe et al. (2022).

with the exception of one $30_\odot$ model of low explosion energy.

In Figure 21, [Ar/O] against [Ne/O] is plotted for the jet-driven models presented in this work and the galaxy (EMPG) data. The horizontal spread of the observed data shows that [Ar/O] is insensitive to [Ne/O], and is higher than the theoretical models. It implies that there are some input physics in the stellar evolutionary models which leads to a systematically smaller [Ar/O]. [Ne/O] has a very small uncertainty. Based on their values, we can infer that the peak progenitor mass that contributes to the observed abundance is between 20 and 25 $M_\odot$. [Ne/O] of these EMPGs suggest that they have the supernova contribution centered around 23 $M_\odot$ stars in their chemical evolution.

We also compare our models with the data points from Isobe et al. (2022) (purple squares with error bars). This element pair also demonstrates a clear clustering for this dataset. The clustering of the data point suggests that these galaxies have a large contribution of the 25 $M_\odot$
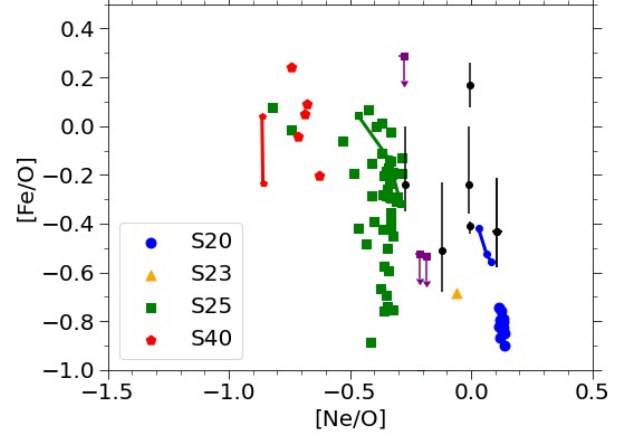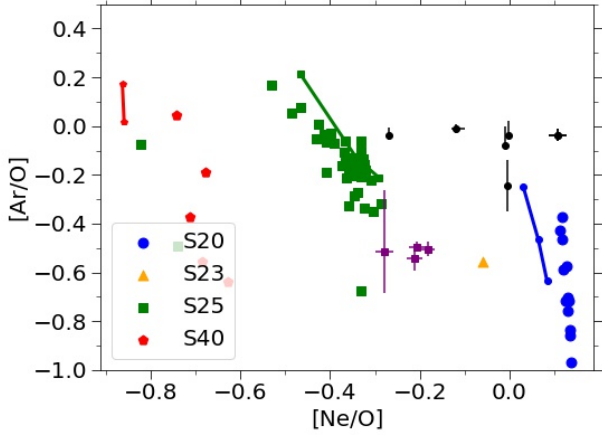
Figure 21. [Ar/O] against [Ne/O] for the jet-driven supernova models in this work, compared with the metal poor galaxy (EMPG) catalog presented in Watanabe et al. (2023) (black circles with error bars) and in Isobe et al. (2022) (purple squares with error bars). The coloured lines stand for the sequence of 1D models with the different explosion energies.
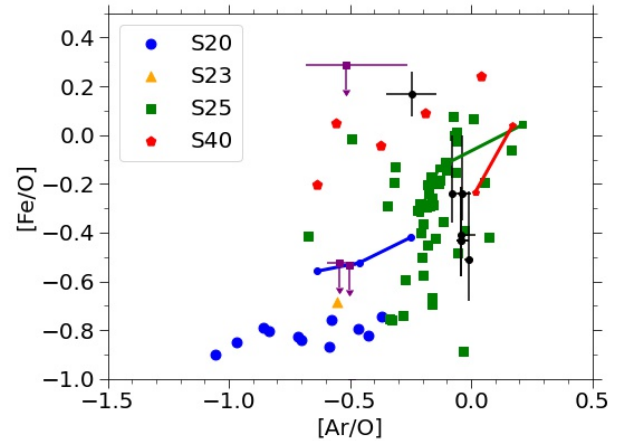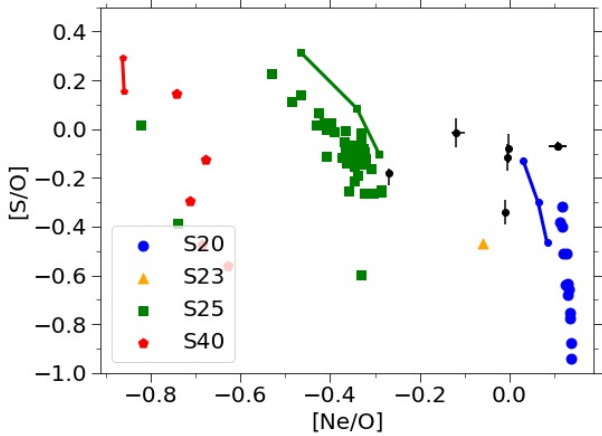

Figure 22. Same as Figure 21 but for [S/O] against [Ne/O].

star explosion in their chemical evolution. The comparison can be similarly made for the data points from (Watanabe et al. 2023) (black circles with error bars). These data points have [Ne/O]$\sim -0.1 - 0.1$, which lie somewhere between the clusters of 20 and 25 $M_\odot$ star explosions. Their high [Ar/O] suggests that these EMPGs require contributions from the high energy explosions of these two groups.

In Figure 22, we plot [S/O] against [Ne/O] for the same sequences of input models. The observational data show that both ratios have a narrow range of $-0.4 - 0.0$, being similar to the solar abundance. The range of [S/O] is consistent with the jet-driven models. The spread
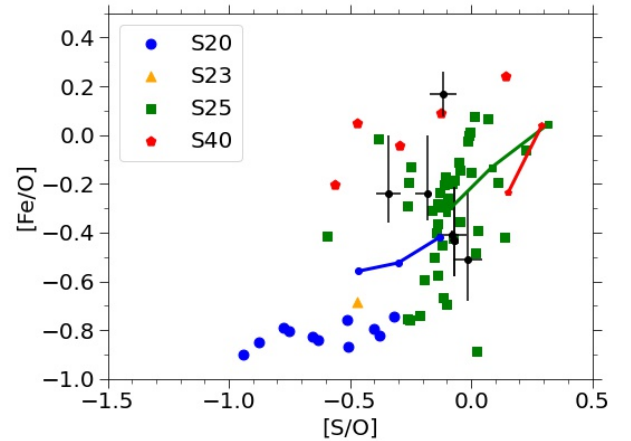
Figure 23. (top panel) Same as Figure 21 but for [Fe/O] against [Ne/O]. (middle panel) Same as the top panel but for [Fe/O] against [Ar/O]. (bottom panel) Same as the top panel but for [Fe/O] against [S/O].

of the S25 models is similar to that for the observed galaxies.

In the top panel of Figure 23, we plot [Fe/O] against [Ne/O] for the same sequences of input models. The observed [Fe/O] shows larger uncertainties compared to the [Ar/O] and [S/O] data. It is interesting to note that, despite the extremely low metallicity in these galaxies, their [Fe/O] does not significantly differ from the solar value. The jet-driven models again produce a spread consistent with the observed range of the abundances ratios.

In the middle panel of the same figure, we compare [Fe/O] against [Ar/O], alongside with the observational data. Different from [Ne/O], the numerical data cluster at [Ar/O] = −1.0 to 0. A smaller mass model tends to have a lower [Ar/O]. The numerical models coincide well with galaxy abundances from Watanabe et al. (2023). There are three galaxies reported in Isobe et al. (2022) and all of them show [Ar/O] around -0.5. The data with low [Fe/O] overlap with the 20 $M_\odot$ spherical explosion models.

The figure can be further compared with the first panel of Figure 2 of Watanabe et al. (2023). In their work, they compare various massive star explosion models with the galaxies they observed. They show that the spherical models requires parametrized "mixing-and-fallback" in order to reproduce the observed abundance ratio, or require contributions of Type Ia supernovae to match the observed [Fe/O]. Our models show that with the jet-driven explosion, the theoretical models may reach the observed high value of [Fe/O].

In the third panel of the same figure, we plot [Fe/O] against [S/O] as in the second panel of Figure 2 of Watanabe et al. (2023). The numerical models show a scatter of [S/O] being similar to [Ar/O], because both elements are Si-group elements. We notice that a lower mass model generates a smaller [S/O]. The 1D models tend to synthesize too much [S/O] but not enough [Fe/O] in this parameter space. In contrast, some galaxy samples match very well with the jet-driven explosion models.

By cross-examining these three figures, it suggests that the aspherical explosion could provide the clue to understand the unique chemical abundance patterns of these metal-poor galaxies.

5.2. *Extremely Metal Poor Stars*

Another ideal test case for massive star nucleosynthesis is extremely metal-poor stars (EMPS). Similar to extremely metal-poor galaxies, the elemental abundances of these old stars correspond to one or a few massive star explosions. The contribution of Type Ia supernovae re-
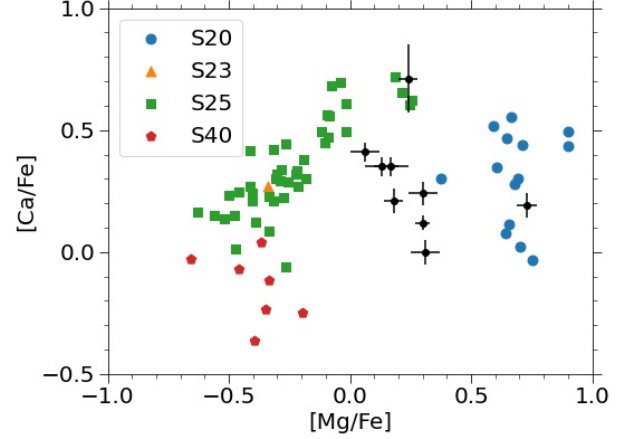

Figure 24. [Ca/Fe] against [Mg/Fe] for the EMPS analyzed in Jeong et al. (2023) (black circle with error bars). Other data points are the theoretical models reported in this work and Leung et al. (2023).

mains less important. However, due to their small length scale, the inhomogeneous mixing and the angle dependence of the aspherical explosion could be important.

Recently, Jeong et al. (2023) made analysis of the high-resolution spectra from stars by the legacy Sloan Digital Sky Survey (SDSS York et al. 2000) and the Large sky Area Multi-Object Fiber Spectroscopic Telescope (LAMOST Cui et al. 2012). They identified 18 very metal-poor stars (VMPS), 10 EMPS and 3 carbon-enhanced metal-poor stars (CEMPS), and perform follow-up observations with the Gemini Remote Access to the CFHT ESPaDOnS Spectrograph (GRACES, Chené et al. 2021). We selected the stars with complete measurement of Mg, Ca, Cr and Ni in Table 7 with a list of stars taken from their catalogue.

In Figure 24, we plot [Ca/Fe] against [Mg/Fe]. Mg is synthesized by C burning and its mass depends on the C/O ratio, which depends on the progenitor mass as is the case of Ne. Thus, this ratio is good for distinguishing the lower mass stars (20 $M_\odot$) and the higher mass stars (25 and 40 $M_\odot$). Different jet deposition schemes provide such a narrow range of [Ca/Fe] variation as $\sim 0 - 0.5$. The observed stellar data are populated between the lower and higher mass groups of stars. This suggests that the abundances in these observed stars were influenced by the produces of stars in the mass range of $20 - 25$ $M_\odot$ (or the mixture of the two classes of explosion). However, one particular EMPS, J2242, has an exceptionally high [Ca/Fe]. None of our models can reproduce such a high value. On the other hand, the EMPS J0010, is likely to be solely influenced by a 20 $M_\odot$ star explosion.

Table 7. Selected extreme metal-poor stars from Jeong et al. (2023). The classification includes VMPS (very metal-poor stars: [Fe/H]< −2), EMPS (extremely metal-poor stars: [Fe/H]< −3), and CEMPS (carbon-enhanced metal-poor stars: [C/Fe]> 1.0).

EMP ID	[Fe/H]	[Mg/Fe]	[Ca/Fe]	[Cr/Fe]	[Ni/Fe]	Classification
J0010	−2.48 ± 0.11	0.73 ± 0.04	0.19 ± 0.05	−0.10 ± 0.05	0.13 ± 0.05	VMPS
J0158	−3.04 ± 0.05	0.06 ± 0.06	0.41 ± 0.04	−0.09 ± 0.06	0.30 ± 0.06	EMPS
J0357	−2.75 ± 0.05	0.34 ± 0.04	0.33 ± 0.03	−0.16 ± 0.05	0.37 ± 0.07	EMPS
J0713	−3.15 ± 0.08	0.31 ± 0.06	0.00 ± 0.05	−0.33 ± 0.03	−0.01 ± 0.04	EMPS
J0814	−3.39 ± 0.05	0.33 ± 0.04	0.61 ± 0.07	−0.33 ± 0.03	−0.01 ± 0.04	EMPS
J0908	−3.67 ± 0.06	0.17 ± 0.07	0.35 ± 0.04	−0.47 ± 0.08	0.35 ± 0.08	EMPS
J1037	−2.50 ± 0.05	0.30 ± 0.03	0.12 ± 0.03	−0.24 ± 0.09	0.34 ± 0.09	CEMPS
J1317	−2.37 ± 0.05	0.30 ± 0.06	0.24 ± 0.05	−0.09 ± 0.11	0.69 ± 0.06	VMPS
J1650	−2.17 ± 0.05	0.13 ± 0.07	0.35 ± 0.04	−0.22 ± 0.10	0.73 ± 0.10	VMPS
J2242	−3.40 ± 0.08	0.24 ± 0.04	0.71 ± 0.14	0.01 ± 0.26	0.89 ± 0.36	EMPS
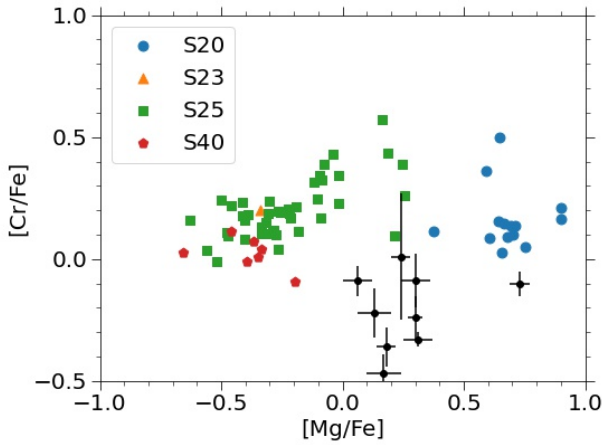
Figure 25. Same as Figure 24 but for [Cr/Fe] against [Mg/Fe].
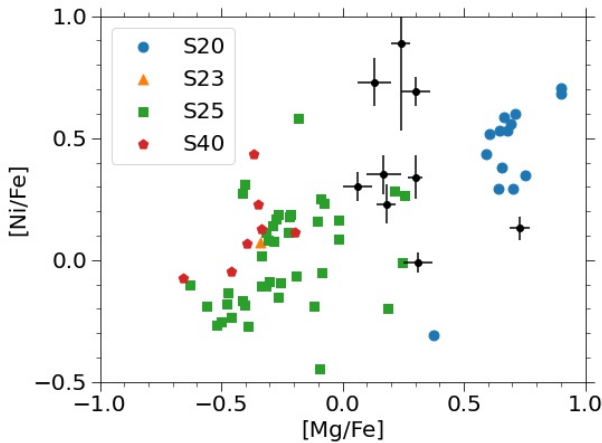
Figure 26. Same as Figure 24 but for [Ni/Fe] against [Mg/Fe].

Figure 25 is similar to Figure 24 but for [Cr/Fe] against [Mg/Fe]. Our models show little variation of [Cr/Fe] across different progenitor and explosion models. Most metal-poor stars selected have [Cr/Fe] similar to the theoretical models, except some has lower value by 0.25 dex.

Figure 26 is similar to Figure 24 but for [Ni/Fe] against [Mg/Fe]. There is a clear distinction between the two classes of models. The lower mass models produce [Ni/Fe] ≳ 0.3, while the higher mass models produce [Ni/Fe] ≲ 0.3. This is related to the initial compactness of the pre-explosion progenitor. A lower mass star has a higher central density, thus undergoing more electron capture. Therefore, the explosion produces more neutron-rich spicies, i.e., ^{58}Ni. Some EMPSs again locate between the two groups, further suggesting the mixed background of massive stars. Some EMPSs exhibit very high [Ni/Fe], e.g., J1317, J1650 and J2242. Since Ni and Fe are synthesized similarly in the inner part of the ejecta, while Cr is produced at further interior part. The high [Ni/Fe] could imply different explosion mechanisms.

5.3. *Metal Poor Star J1010+2358*

The Galactic halo star J1010+2358 was discovered by the LAMOST survey (Large Sky Area Multi-Object Fiber Spectroscopic Telescope; Zhao et al. 2006, 2012), and confirmed to be a very metal poor star (VMPS) with [Fe/H] = −2.42. It has an unusually low [Mg/Fe] ∼ −0.66, which makes it distinctive from typical Galactic halo stars. In the recent observation by Xing et al. (2023), element ratios against Fe, including Mg, Si, Ca, Ti, Cr, Mn, Fe, Co and Ni are reported. The low [Mg/Fe] and [Mn/Mg] suggests less contribution from Type Ia supernovae and canonical core-collapse supernovae. A high mass CCSN produces too high [Mn/Fe] and [Co/Fe] which are less compatible with the observed abundances. They further show that the yield patterns

are compatible with the 260 $M_\odot$ pair-instability super-novae in Heger & Woosley (2002).

In that work, the spherical explosion models are compared with this VMP star. Since our models suggest that the aspherical explosion by the jet can lead to distinctive chemical abundance patterns. Here, we extend the search to our jet-driven supernova models. We use the measured elements as the constraints, and look for the best-fit models.

In Figure 27 we show such comparisons. For each massive star progenitor, we search for the best-fit models with the minimum χ-square. For 1D models, because there is no variation in the explosion, we compare among all progenitors with different explosion energies. In Table 8 we list our comparison results. It shows that the parameters close to the characteristic model can already provide a close fit to this object. The best-fit model is found for $M_{\mathrm{ZAMS}} = 25\ M_\odot$.

Our best-fit model S25-2000-1000-30 shows that the suppressed [Mg/Fe], sub-solar [Mn/Fe] and [Co/Fe] are reproduced to a good accuracy. There is an underproduction of Si relative to Fe, and an overproduction of Ti and Cr. Na/Fe, Sc/Fe and Zn/Fe also agree with the observed upper limits. The low [Mn/Fe] and [Co/Fe] can be reproduced by aspherical explosions of much lower mass stars ($\sim 25\ M_\odot$ compared with 260 $M_\odot$. On the other hand, the 20 and 40 $M_\odot$ can provide a fit similar to the 25 $M_\odot$ model.

The S20 model is close to the S25 but the [Mg/Fe] and [Mn/Fe] are significantly overproduced. While [Ni/Fe] and [Zn/Fe] agrees with the observational data, the underproduction of Si and Ca can be seen. A similar problem appears for the S40 model. The underproduction of Si and Ca persists, while there is a severe overproduction of Mn, Ni. Minor elements such as Sc and Zn also overproduced compared to the upper limits. In both models, the mismatch of Ti/Fe and Cr/Fe can be also found as in S25.

The best-fit 1D model shows the overproduction of [Co/Fe] and [Ni/Fe]. This is expected due to the complete ejection of the Fe-rich layer during the explosion. The overproduction in minor elements including [Sc/Fe] and [Zn/Fe] persists. The systematic higher [Ti/Fe] and [Cr/Fe] among all progenitor models suggest the inherent dependence on how the massive star progenitor is evolved.

The object is extensively compared in Xing et al. (2023). The comparison with the Chandrasekhar mass white dwarf yields are used to compare with this VMP star. However, in such an early system, we expect that the contribution from the Chandrasekhar mass white dwarf explosion is low because of the time delay from

Table 8. The best-fit models from our numerical models based on each massive star progenitors. The column "Explosion" stands for whether the 2D-jet or the 1D spherical explosion is used. The Model is the best-fit model for that progenitor.

Explosion	M_{ZAMS}	Model	χ^2
Jet	20	S20-0250-1000-15	17.6
Jet	25	S25-1000-0250-15	15.5
Jet	40	S40-1000-1000-15	16.6
Spherical	30	$E_{\mathrm{exp}} = 1 \times 10^{52}$ erg	25.8

the formation of the white dwarf until it reaches the ignition mass (Kobayashi et al. 2020). In fact, the sub-Chandrasekhar mass Type Ia supernova yields in Leung & Nomoto (2020) show low or sub-solar [Ti/Fe], [Cr/Fe], [Mn/Fe] and [Co/Fe] in contrast to the Chandrasekhar mass counterpart (see e.g., Nomoto & Leung 2017, 2018; Leung & Nomoto 2018). The mixing of yields of jet-driven supernovae with the low metallicity sub-Chandrasekhar models can lead to lower mass fraction ratios in Ti and Cr.

Given the strong mass dependence of [Ne/O] as demonstrated in the previous section, the knowledge of spectral data from lines of these two elements will provide important insights for determining the origin of the supernova (1D vs. 2D CCSN, PISN).

6. CONCLUSION

In this article, we compare nucleosynthesis yields of our jet-driven supernova models using multi-dimensional simulations. We calculate explosions of massive stars from $20 - 40\ M_\odot$ and compute their explosive nucleosynthesis. We study how the explosion hydrodynamics and nucleosynthesis depend on the progenitor properties (mass, mass cut and dimensionality). We compare the ejecta observable, including chemical abundances with available metal-poor stars, supernova surveys and metal-poor galaxies. Some of our models are consistent with the recently observed extremely metal-poor galaxies (EMPGs). Below we list our finding of this work:

1. The inner mass cut and the initial black hole mass strongly change the [Fe/O] ratio of the ejecta and the ejecta mass.

2. Asphericity of the explosion provides a reasonable energy budget to match the high velocity, and the thermodynamics history is distinct from the spherical counterpart.

3. The spread of the explosion energetics can explain the diversity of the observed supernova ejecta mass
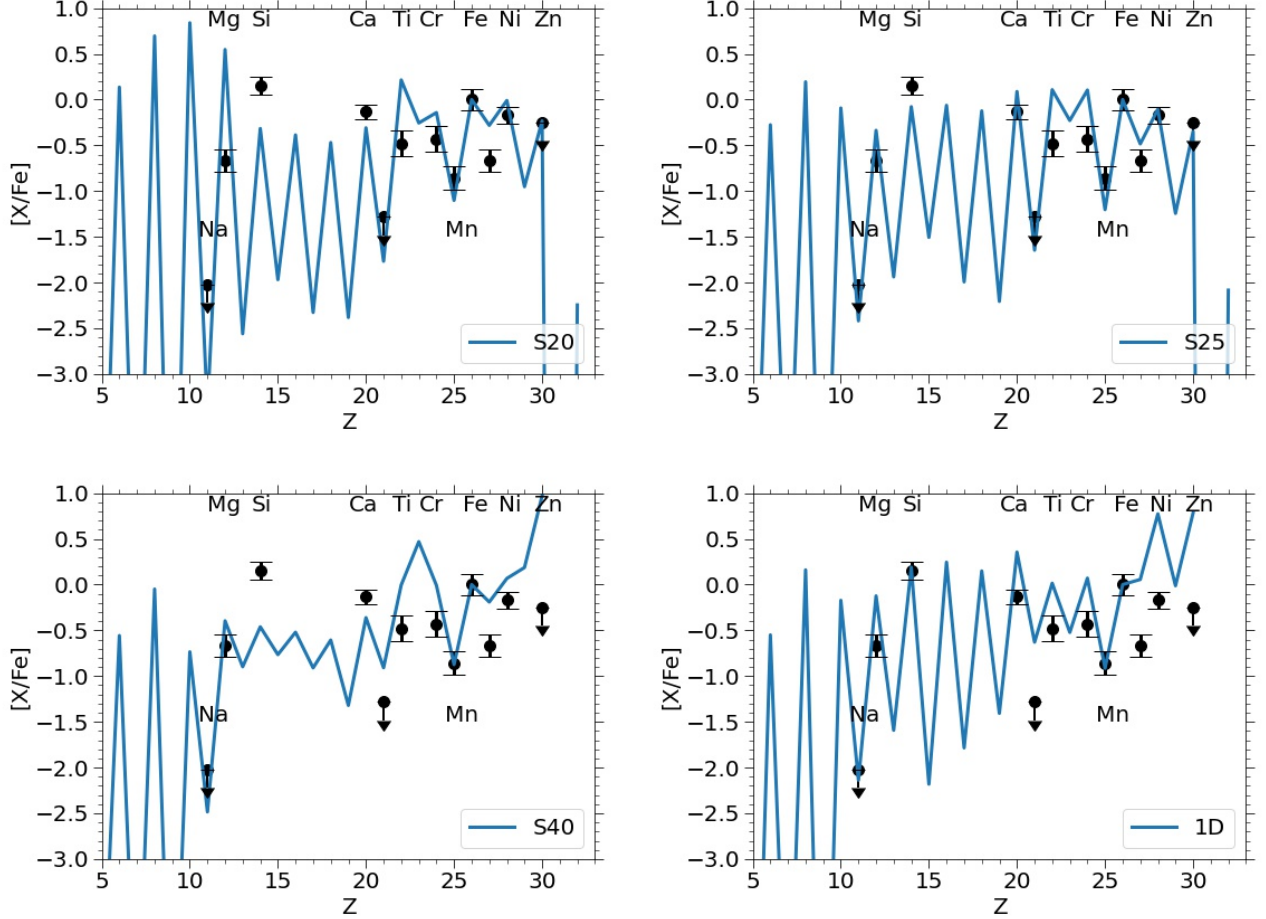
Figure 27. (top left panel) The chemical abundance of J1010+2358 (circles with error bars) and the best-fit models S20-0250-1000-15 from our jet-driven supernova models with $M_{\rm prog} = 20\ M_\odot$. (top right panel) Same as the top left panel, but for $M_{\rm prog} = 25\ M_\odot$ with the model S25-1000-0250-15. (bottom left panel) Same as the top left panel, but for $M_{\rm prog} = 40\ M_\odot$ with the Model S40-1000-1000-15. (bottom right panel) Same as the top left panel, but for all 1D models, with the best-fit model by the progenitor $30 M_\odot$ with an explosion energy of 1×10^{52} erg.

and ^{56}Ni distribution. Some parameter space featuring extremely high ^{56}Ni ($> 1\ M_\odot$) and high ejecta mass $\sim 10\ M_\odot$ remains to be solved.

4. The lower mass ($\sim 25\ M_\odot$) models can produce the Ti-V relation consistent with that from the metal-poor stars in the stellar survey in the literature.

5. The extremely metal-poor galaxies can be characterized by their [Ne/O] which is sensitive to the progenitor mass. A high [Ne/O] corresponds to a lower progenitor mass and vice versa.

6. The Very Metal Poor star J1010+2358 in the Galactic Halo, poor in [Mg/Fe] and [Mn/Fe] can be well matched with our jet-driven supernova of our 25 $M_\odot$ progenitor.

7. Despite the extremely metal-poor nature, i.e., even without contribution of Type Ia supernovae, the abundance ratios [(Fe, Ca, Ar, S, Si)/O] of these EMPGs are comparable with the solar values, which can be matched with single or a few jet-induced supernova explosions.

8. Metal-poor stars tend to exhibit the abundance pattern a mixture of multiple supernova explosions instead of a single one.

ACKNOWLEDGEMENT

REFERENCES

Arnett, D., Fryxell, B., & Mueller, E. 1989, ApJL, 341, L63, doi: 10.1086/185458

Chené, A.-N., Mao, S., Lundquist, M., et al. 2021, AJ, 161, 109, doi: 10.3847/1538-3881/abd411

Couch, S. M., Wheeler, J. C., & Milosavljević, M. 2009, ApJ, 696, 953, doi: 10.1088/0004-637X/696/1/953

Cui, X.-Q., Zhao, Y.-H., Chu, Y.-Q., et al. 2012, Research in Astronomy and Astrophysics, 12, 1197, doi: 10.1088/1674-4527/12/9/003

De Cia, A., Gal-Yam, A., Rubin, A., et al. 2018, ApJ, 860, 100, doi: 10.3847/1538-4357/aab9b6

Ezzeddine, R., Frebel, A., Roederer, I. U., et al. 2019, ApJ, 876, 97, doi: 10.3847/1538-4357/ab14e7

Gomez, S., Berger, E., Nicholl, M., Blanchard, P. K., & Hosseinzadeh, G. 2022, ApJ, 941, 107, doi: 10.3847/1538-4357/ac9842

Hachisu, I., Matsuda, T., Nomoto, K., & Shigeyama, T. 1990, ApJL, 358, L57, doi: 10.1086/185779

Hartwig, T., Yoshida, N., Magg, M., et al. 2018, MNRAS, 478, 1795, doi: 10.1093/mnras/sty1176

Heger, A., & Woosley, S. E. 2002, ApJ, 567, 532, doi: 10.1086/338487

Hirano, S., Hosokawa, T., Yoshida, N., Omukai, K., & Yorke, H. W. 2015, MNRAS, 448, 568, doi: 10.1093/mnras/stv044

Höflich, P., Wheeler, J. C., & Wang, L. 1999, ApJ, 521, 179, doi: 10.1086/307521

Ishigaki, M. N., Tominaga, N., Kobayashi, C., & Nomoto, K. 2018, ApJ, 857, 46, doi: 10.3847/1538-4357/aab3de

Isobe, Y., Ouchi, M., Suzuki, A., et al. 2022, ApJ, 925, 111, doi: 10.3847/1538-4357/ac3509

Iwamoto, N., Umeda, H., Tominaga, N., Nomoto, K., & Maeda, K. 2005, Science, 309, 451, doi: 10.1126/science.1112997

Izotov, Y. I., Thuan, T. X., Guseva, N. G., & Liss, S. E. 2018, MNRAS, 473, 1956, doi: 10.1093/mnras/stx2478

Jeong, M., Lee, Y. S., Beers, T. C., et al. 2023, arXiv e-prints, arXiv:2301.06236, doi: 10.48550/arXiv.2301.06236

Kobayashi, C., Leung, S.-C., & Nomoto, K. 2020, ApJ, 895, 138, doi: 10.3847/1538-4357/ab8e44

Kojima, T., Ouchi, M., Rauch, M., et al. 2020, ApJ, 898, 142, doi: 10.3847/1538-4357/aba047

Latif, M. A., Whalen, D., & Khochfar, S. 2022, ApJ, 925, 28, doi: 10.3847/1538-4357/ac3916

Leung, S. C., Chu, M. C., & Lin, L. M. 2015, MNRAS, 454, 1238, doi: 10.1093/mnras/stv1923

Leung, S.-C., & Nomoto, K. 2018, ApJ, 861, 143, doi: 10.3847/1538-4357/aac2df

—. 2020, ApJ, 888, 80, doi: 10.3847/1538-4357/ab5c1f

Leung, S.-C., & Nomoto, K. 2023, in The Sixteenth Marcel Grossmann Meeting. On Recent Developments in Theoretical and Experimental General Relativity, 4427–4446, doi: 10.1142/9789811269776_0374

Leung, S.-C., Nomoto, K., & Suzuki, T. 2023, ApJ, 948, 80, doi: 10.3847/1538-4357/acbdf5

Maeda, K., Mazzali, P. A., & Nomoto, K. 2006, ApJ, 645, 1331, doi: 10.1086/504581

Maeda, K., Nakamura, T., Nomoto, K., et al. 2002, ApJ, 565, 405, doi: 10.1086/324487

Mao, J., Zhou, P., Simionescu, A., et al. 2021, ApJL, 918, L17, doi: 10.3847/2041-8213/ac1945

Marigo, P., Girardi, L., Chiosi, C., & Wood, P. R. 2001, A&A, 371, 152, doi: 10.1051/0004-6361:20010309

Mazzali, P. A., Nomoto, K., Patat, F., & Maeda, K. 2001, ApJ, 559, 1047, doi: 10.1086/322420

Mazzali, P. A., Kawabata, K. S., Maeda, K., et al. 2005, Science, 308, 1284, doi: 10.1126/science.1111384

Murphy, L. J., Groh, J. H., Ekström, S., et al. 2021, MNRAS, 501, 2745, doi: 10.1093/mnras/staa3803

Nagataki, S., Hashimoto, M.-a., Sato, K., & Yamada, S. 1997, ApJ, 486, 1026, doi: 10.1086/304565

Nagataki, S., Shimizu, T. M., & Sato, K. 1998, ApJ, 495, 413, doi: 10.1086/305258

Nakamura, T., Mazzali, P. A., Nomoto, K., & Iwamoto, K. 2001, ApJ, 550, 991, doi: 10.1086/319784

Nomoto, K., Kobayashi, C., & Tominaga, N. 2013, ARA&A, 51, 457, doi: 10.1146/annurev-astro-082812-140956

Nomoto, K., & Leung, S.-C. 2017, in Handbook of Supernovae, ed. A. W. Alsabti & P. Murdin (Springer Verlag AG: Cham), 1275, doi: 10.1007/978-3-319-21846-5_62

—. 2018, SSRv, 214, 67, doi: 10.1007/s11214-018-0499-0

Roederer, I. U., Preston, G. W., Thompson, I. B., et al. 2014, AJ, 147, 136, doi: 10.1088/0004-6256/147/6/136

Seitenzahl, I. R., Röpke, F. K., Fink, M., & Pakmor, R. 2010, MNRAS, 407, 2297, doi: 10.1111/j.1365-2966.2010.17106.x

Sneden, C., Cowan, J. J., Kobayashi, C., et al. 2016, ApJ, 817, 53, doi: 10.3847/0004-637X/817/1/53

Sukhbold, T., Ertl, T., Woosley, S. E., Brown, J. M., & Janka, H. T. 2016, ApJ, 821, 38, doi: 10.3847/0004-637X/821/1/38

Taddia, F., Sollerman, J., Fremling, C., et al. 2019, A&A, 621, A71, doi: 10.1051/0004-6361/201834429

Timmes, F. X. 1999, ApJS, 124, 241, doi: 10.1086/313257

Timmes, F. X., & Arnett, D. 1999, ApJS, 125, 277, doi: 10.1086/313271

Timmes, F. X., Hoffman, R. D., & Woosley, S. E. 2000, ApJS, 129, 377, doi: 10.1086/313407

Timmes, F. X., & Swesty, F. D. 2000, ApJS, 126, 501, doi: 10.1086/313304

Tominaga, N. 2009, ApJ, 690, 526, doi: 10.1088/0004-637X/690/1/526

Tominaga, N., Maeda, K., Umeda, H., et al. 2007a, ApJL, 657, L77, doi: 10.1086/513193

Tominaga, N., Umeda, H., & Nomoto, K. 2007b, ApJ, 660, 516, doi: 10.1086/513063

Travaglio, C., Hillebrandt, W., Reinecke, M., & Thielemann, F. K. 2004, A&A, 425, 1029, doi: 10.1051/0004-6361:20041108

Umeda, H., & Nomoto, K. 2002, ApJ, 565, 385, doi: 10.1086/323946

Watanabe, K., Ouchi, M., Nakajima, K., et al. 2023, ApJ, in press, arXiv:2305.02078, doi: 10.48550/arXiv.2305.02078

Weaver, T. A., Zimmerman, G. B., & Woosley, S. E. 1978, ApJ, 225, 1021, doi: 10.1086/156569

Woosley, S. E., & Weaver, T. A. 1995, ApJS, 101, 181, doi: 10.1086/192237

Xing, Q.-F., Gang, Z., Liu, Z.-W., et al. 2023, Nature, 1, doi: 10.1038/s41586-023-06028-1

York, D. G., Adelman, J., Anderson, John E., J., et al. 2000, AJ, 120, 1579, doi: 10.1086/301513

Zhao, G., Chen, Y.-Q., Shi, J.-R., et al. 2006, ChJA&A, 6, 265, doi: 10.1088/1009-9271/6/3/01

Zhao, G., Zhao, Y.-H., Chu, Y.-Q., Jing, Y.-P., & Deng, L.-C. 2012, Research in Astronomy and Astrophysics, 12, 723, doi: 10.1088/1674-4527/12/7/002